Received: 24 January 2023 | Revised: 23 May 2023 | Accepted: 26 May 2023

DOI: 10.1111/bre.12789

RESEARCH ARTICLE

Basin Research | IAS EAGE | WILEY

Basin scale evolution of zebra textures in fault-controlled, hydrothermal dolomite bodies: Insights from the Western Canadian Sedimentary Basin

Cole A. McCormick[1] | **Hilary Corlett**[2] | **Matthieu Clog**[3] | **Adrian J. Boyce**[3] | **Romain Tartèse**[1] | **Matthew Steele-MacInnis**[4] | **Cathy Hollis**[1]

[1]Department of Earth and Environmental Sciences, The University of Manchester, Manchester, UK

[2]Department of Earth Sciences, Memorial University of Newfoundland, St. John's, Newfoundland, Canada

[3]Scottish Universities Environmental Research Council, Glasgow, UK

[4]Department of Earth and Atmospheric Sciences, University of Alberta, Edmonton, Alberta, Canada

Correspondence
Cole A. McCormick, Department of Earth and Environmental Sciences, The University of Manchester, Manchester M13 9PL, UK.
Email: cole.mccormick@manchester.ac.uk

Funding information
American Association of Petroleum Geologists Foundation; British Sedimentological Research Group; International Association of Sedimentologists; Natural Environment Research Council (NERC); President's Doctoral Scholar Award (The University of Manchester); Society for Sedimentary Geology Foundation

Abstract

Structurally controlled dolomitization typically involves the interaction of high-pressure (P), high-temperature (T) fluids with the surrounding host rock. Such reactions are often accompanied by cementation and recrystallization, with the resulting hydrothermal dolomite (HTD) bodies including several 'diagnostic' rock textures. Zebra textures, associated with boxwork textures and dolomite breccias, are widely considered to reflect these elevated P/T conditions. Although a range of conceptual models have been proposed to explain the genesis of these rock textures, the processes that control their spatial and temporal evolution are still poorly understood. Through the detailed petrographical and geochemical analysis of HTD bodies, hosted in the Middle Cambrian strata in the Western Canadian Sedimentary Basin, this study demonstrates that a single genetic model cannot be applied to all the characteristics of these rock textures. Instead, a wide array of sedimentological, tectonic and metasomatic processes contribute to their formation; each of which is spatially and temporally variable at the basin scale. Distal to the fluid source, dolomitization is largely stratabound, comprising replacement dolomite, bedding-parallel zebra textures and rare dolomite breccias (non-stratabound, located only proximal to faults). Dolomitization is increasingly non-stratabound with proximity to the fluid source, comprising bedding-inclined zebra textures, boxwork textures and dolomite breccias that have been affected by recrystallization. Petrographical and geochemical evidence suggests that these rock textures were initiated due to dilatational fracturing, brecciation and precipitation of saddle dolomite as a cement, but significant recrystallization occurred during the later stages of dolomitization. These rock textures are closely associated with faults and carbonate-hosted ore deposits (e.g. magnesite, rare earth element and Mississippi Valley–type mineralization), thus providing invaluable information regarding fluid flux and carbonate metasomatism under elevated P/T conditions.

KEYWORDS
clumped isotope thermometry, fault-controlled dolomitization, rare earth element analysis, recrystallization, saddle dolomite, zebra texture

1 | INTRODUCTION

Dolomitization refers to the replacement (crystal scale dissolution-precipitation sensu Putnis, 2002) of $CaCO_3$ by $CaMg(CO_3)_2$, expressed as:

$$2CaCO_3\,(s) + Mg^{2+}\,(aq) \rightleftharpoons CaMg(CO_3)_2\,(s) + Ca^{2+}\,(aq) \quad (1)$$

Dolomite cementation is different from dolomitization and refers to the precipitation of $CaMg(CO_3)_2$ directly from an aqueous solution (sensu Machel, 2004):

$$Ca^{2+}\,(aq) + Mg^{2+}\,(aq) + 2CO_3{}^{2-}\,(aq) \rightleftharpoons CaMg(CO_3)_2\,(s) \quad (2)$$

Dolomite recrystallization is a broad term that includes both low temperature diagenetic recrystallization (replacement of pre-existing crystals by new, thermodynamically stable, crystals of the same mineralogy sensu Machel, 1997) and high temperature dynamic recrystallization (by grain boundary migration sensu Newman & Mitra, 1994).

Fault-controlled, hydrothermal dolomitization is an important metasomatic reaction in the Earth's upper crust that involves the replacement of $CaCO_3$ by $CaMg(CO_3)_2$, mediated by an aqueous solution that is of higher temperature than the ambient host rock (Davies & Smith, 2006; Machel & Lonnee, 2002). The resulting hydrothermal dolomite (HTD) bodies are economically significant because they can form reservoirs for energy exploitation and carbon storage, and they commonly host Mississippi Valley–type mineralization (Duggan et al., 2001; Paradis & Simandl, 2017; Vandeginste et al., 2007). Fault-controlled dolomitization is accompanied by multiple phases of cementation and recrystallization that fingerprint the evolving fluid composition of a sedimentary basin, alongside the timing, depth and temperature that contributed to these reactions (Koeshidayatullah et al., 2020; Lonnee & Machel, 2006; Martín-Martín et al., 2015). Certain rock textures (e.g. zebra textures, boxwork textures and dolomite breccias) are common in fault-controlled dolomite bodies and are often considered to be diagnostic of HTD because their presence has been interpreted to be evidence of elevated P/T conditions (Boni et al., 2000; Breislin et al., 2022; Centrella et al., 2022; Iannace et al., 2012; Kareem et al., 2019; Nielsen et al., 1998; Vandeginste et al., 2005). Nevertheless, HTD can form without these rock textures (Hendry et al., 2015; Hirani et al., 2018; Hollis et al., 2017; Rustichelli et al., 2017), and there is still controversy regarding the mechanism(s) by which they form (Wallace & Hood, 2018, and references therein).

Highlights

- The basin scale distribution and characteristics of zebra textures are controlled by sedimentological, tectonic and metasomatic processes.
- The product(s) of these mechanisms are spatially and temporally variable based on their proximity to the source of the dolomitizing fluid.
- Zebra textures are initiated as fractures, with clear evidence of dilatation and cementation.
- These fractures can be reactivated to facilitate successive pulses of the dolomitizing fluid.
- Successive fluid pulses also contribute to recrystallization, forming increasingly complex rock textures.

Zebra textures comprise alternating, mm- to cm-scale, bands of replacement dolomite (RD) and saddle dolomite (SD) that form symmetrical RD-SD-SD-RD patterns. These rock textures are closely associated with boxwork textures that are similarly banded but with highly irregular orientations, as well as dolomite breccias that include floating clasts of RD that are fully surrounded and supported by SD. Earlier works suggested that zebra textures form through the preferential dissolution of carbonate or evaporitic sedimentary rocks, where the dark, finely crystalline bands form through replacement of the carbonate host rock and the light, coarsely crystalline bands are cement-filled cavities (Beales & Hardy, 1980; Fontboté & Gorzawski, 1990; Krebs & Macqueen, 1984; Morrow, 2014). More recent studies, however, have suggested that fracturing is the dominant process by which these cavities are generated (Hiemstra & Goldstein, 2015; López-Horgue et al., 2009; Nielsen et al., 1998; Swennen et al., 2003; Wallace et al., 1994; Wallace & Hood, 2018), with zebra textures reported in a wide range of compressional (Gabellone et al., 2014; Gasparrini et al., 2006; Iannace et al., 2012; Kareem et al., 2019; Sharp et al., 2010; Vandeginste et al., 2014), strike-slip (Dewit et al., 2014; López-Horgue et al., 2010; Swennen et al., 2012) and extensional (Boni et al., 2000; Shelton et al., 2019; Stacey et al., 2021) tectonic settings. A smaller number of studies

have also recognized the importance of recrystallization on the formation of these rock textures, at P/T conditions approaching low-grade metamorphism (Centrella et al., 2022; Kelka et al., 2015, 2017). The wide range of models that have been proposed to explain the genesis of zebra textures can be grouped into (i) sedimentological models (i.e. influenced by precursor sedimentological characteristics), (ii) tectonic models (i.e. formed by fracturing) and (iii) metasomatic models (i.e. formed by replacement and/or recrystallization). Given the wide disparities between these interpretations, it is unclear what exactly these rock textures are 'diagnostic' of. In particular, many of the observations that are used to support a given model do not refute the others, which highlights the possibility that zebra textures, boxwork textures and dolomite breccias may form due to a combination of several processes.

The vertically and laterally extensive exposures of HTD bodies in the southern Rocky Mountains, hosted in the Cathedral Formation and the Eldon Formation (Middle Cambrian; Miaolingian Epoch; 509 to 497 Ma) in the Western Canadian Sedimentary Basin (WCSB), offer an unparalleled natural laboratory to unravel the controls on basin scale (tens to hundreds of kilometres in extent), fault-controlled fluid flow and the resulting dolomitization patterns. Such a basin scale approach is rarely possible, with many studies focusing on individual outcrops and a small number of samples, but with rigorous detail at the microscopic scale. By integrating a suite of field, petrographical and geochemical data across a carbonate platform that was hundreds of kilometres wide, this study aims to elucidate the genesis of zebra textures, boxwork textures and dolomite breccias in the WCSB. We evaluate the sedimentological, tectonic and metasomatic models that have been proposed to explain the genesis of these rock textures (at the micrometre to centimetre scale), while highlighting their spatial and temporal evolution relative to the source of the dolomitizing fluid (at the meter to kilometre scale).

2 | GEOLOGICAL SETTING

2.1 | Tectonic setting

The WCSB includes a southwest-thickening wedge of sedimentary rocks, up to ca. 18 km thick, that extend from the southwest corner of the Northwest Territories to the north-central United States (Figure 1a,b). In the southern Rocky Mountains, the WCSB includes four unconformity-bounded packages of strata that are informally divided based on their tectonic settings. The Purcell Supergroup (Mesoproterozoic) records deposition in an intracratonic basin, whereas the Windermere Supergroup (Neoproterozoic) records the rifting of Laurentia. Lower Cambrian (Terreneuvian Epoch to Series 2; 541 to 509 Ma) to Triassic strata were deposited on what was considered a passive margin (Aitken, 1989; Bond & Kominz, 1984; Slind et al., 1994), although tectonic activity and heat flow likely remained high during the Cambrian (Bond et al., 1985; Johnston et al., 2009; Powell et al., 2006). Jurassic to Palaeocene strata record the transition to a foreland basin during the Columbian and Laramide orogenies.

The modern structure of the southern Rocky Mountains is dominated by E-NE verging thrust faults that formed during the Antler, Columbian and Laramide orogenies (McMechan, 2022; Price, 1981; Root, 2001). However, there are several pre-orogenic structural elements in the southern Rocky Mountains, including NE–SW trending normal and transtensional faults that intersect Middle Cambrian strata (Davies & Smith, 2006; Stacey et al., 2021). The most prominent of these early structural features is the Kicking Horse Rim (oriented N-NW), an elevated paleotopographic feature that formed due to the syn-depositional reactivation of deep-rooted basement faults and influenced the position of the carbonate platform margin during the Cambrian and Ordovician (Aitken, 1971, 1989, 1997; Collom et al., 2009).

2.2 | Stratigraphy

Middle Cambrian strata in the southern Rocky Mountains record a series of northeast-transgressing carbonate-mudrock cycles that comprise regionally extensive facies belts (Figure 1c; Aitken, 1989, 1997). These cycles include a central carbonate platform-shoal complex that grades laterally into proximal slope facies to the southwest and intrashelf basin facies to the northeast (Figure 1d; Aitken, 1989, 1997; Pratt, 2002). Throughout the Middle Cambrian, each of the carbonate platform-shoal complexes were paleogeographically confined by the tectonically active Kicking Horse Rim (Aitken, 1971), and the development of each platform terminated due to the collapse of its basinward margin, platform drowning and burial by siliciclastic sediment (Aitken, 1989; Collom et al., 2009; Johnston et al., 2009). Consequently, the facies at the Kicking Horse Rim locality (51°26′11.5″N, 116°22′48.5″W) represent a platform margin environment, whereas those at the Whirlpool Point locality (52°00′07.5″N, 116°28′13.5″W) represent a platform interior environment (Aitken, 1989; Pratt, 2002).

The Cathedral Formation (limestone, stratabound and non-stratabound dolomite) overlies the Mount Whyte Formation (argillaceous limestone, shale, dolomite)

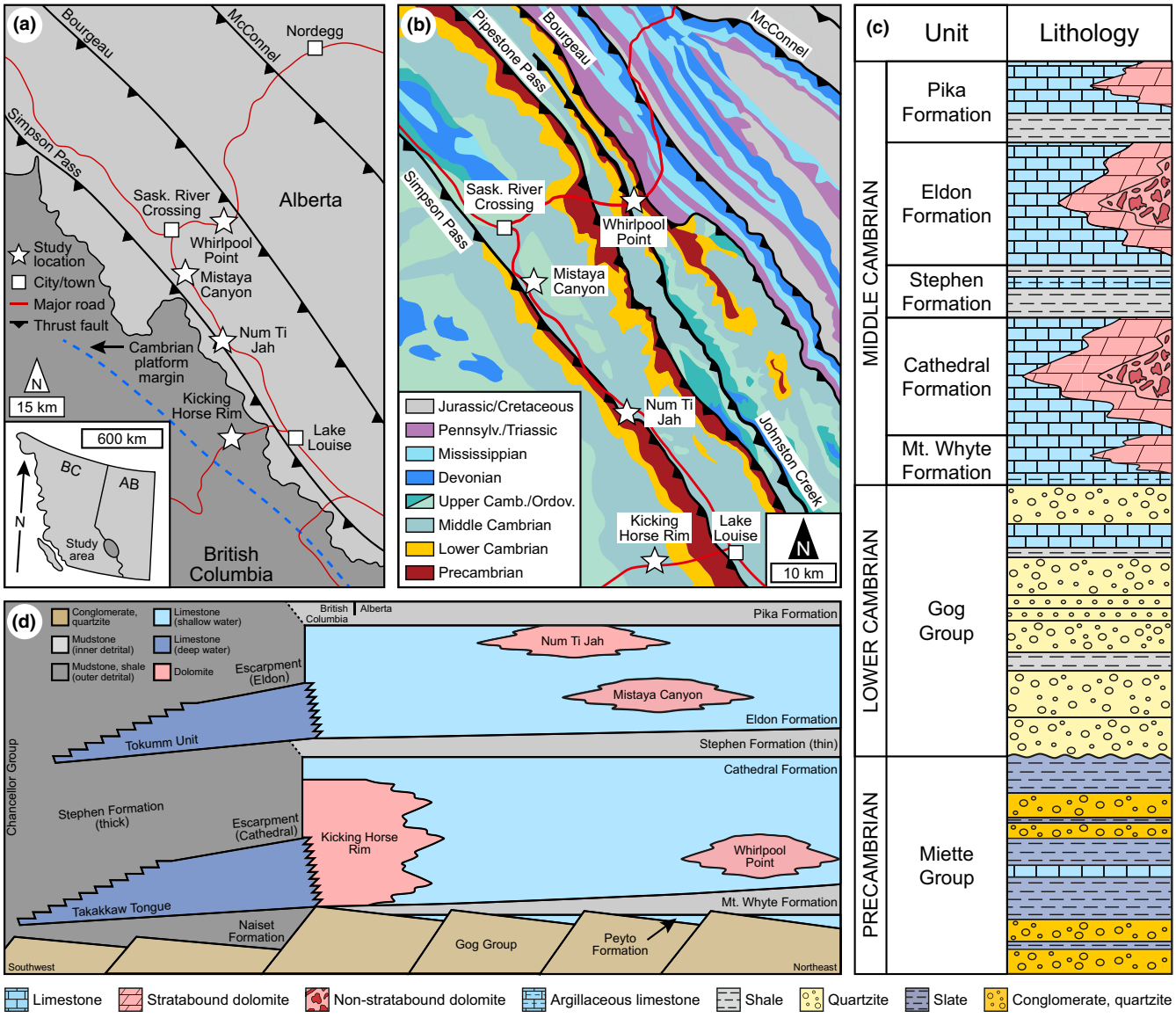

FIGURE 1 (a) Location of the study area in the southern Rocky Mountains (WCSB) showing the major thrust faults and the Cambrian platform margin (modified from Stacey et al., 2021; based on Wheeler et al., 1996). (b) Geological map of the study area (modified from Stacey et al., 2021; based on the Alberta Geological Survey Interactive Minerals Map: https://ags.aer.ca/publication/iam-001). (c) Stratigraphy of the southern Rocky Mountains (based on Aitken, 1997). (d) Schematic cross-section of the Middle Cambrian strata in the southern Rocky Mountains (modified from Collom et al., 2009).

at Whirlpool Point, whereas it overlies the Gog Group (quartzite, shale) at the Kicking Horse Rim (Aitken, 1997; Koeshidayatullah et al., 2020). The Cathedral Formation is up to 610 m thick at its platform margin on Mount Stephen, thinning to the northeast (Aitken, 1997). The Cathedral Formation is overlain by the Stephen Formation (shale, argillaceous limestone), which is 103 m thick at its type section on Mount Bosworth (Aitken, 1997). The Stephen Formation is overlain by the Eldon Formation (limestone, stratabound and non-stratabound dolomite), which is up to 488 m thick at its platform margin (Aitken, 1997), and the Eldon Formation is overlain by the Pika Formation (argillaceous limestone, shale, dolomite). The Cathedral Formation outcrops at Whirlpool Point in the Bourgeau Thrust and at the Kicking Horse Rim in the Simpson Pass. The Eldon Formation outcrops at the Mistaya Canyon (51°55′09.5″N, 116°43′23.5″W) and the Num Ti Jah (51°39′13.0″N, 116°29′59.0″W) localities in the Pipestone Pass (Figure 1b,c).

2.3 | Spatial and temporal evolution of hydrothermal dolomite bodies

Over the past several years, considerable progress has been made in the understanding of the spatial and

temporal evolution of HTD bodies (Benjakul et al., 2020; Centrella et al., 2021; Humphrey et al., 2022; Koeshidayatullah et al., 2021; Yao et al., 2020). Of particular relevance to the Middle Cambrian strata in the WCSB is the recognition that dolomitization is self-limiting due to the (i) abrupt reduction of the Mg/Ca ratio at the dolomitization front and (ii) decreased permeability proximal to the source of the dolomitizing fluid (Koeshidayatullah et al., 2020). Dolomitization of the Middle Cambrian strata in the WCSB has been shown to be hydrothermal in origin; forming in a shallow to intermediate burial environment at temperatures that are >150°C (Koeshidayatullah et al., 2020; Stacey et al., 2021). In these systems, the dolomitization front 'retreats' over time due to the recrystallization of earlier paragenetic stages as each successive fluid pulse enters the strata. Such recrystallization occludes porosity and results in the core of the HTD body being younger than its margins. This phenomenon can be recognized by the spatial distribution of each paragenetic stage in the strata (McCormick et al., 2021), alongside a systematic increase in the dolomitization temperature and $\delta^{18}O_{fluid}$ values towards the core of the HTD body (Koeshidayatullah et al., 2020). Recrystallization coincides with the shift from zoned, planar-e dolomite (distal to the fluid source) to unzoned, planar-s to nonplanar dolomite (proximal to the fluid source). Such relationships have been established at the outcrop scale (Koeshidayatullah et al., 2020; Koeshidayatullah et al., 2021; McCormick et al., 2021; Stacey et al., 2021), but whether they hold true at the basin scale is equivocal. Likewise, the relationship between these dolomitization patterns and the formation of zebra textures, boxwork textures and dolomite breccias has not been investigated.

3 | METHODS

Ninety-two representative samples were collected from Whirlpool Point ($n=35$), Mistaya Canyon ($n=30$), Num Ti Jah ($n=9$) and the Kicking Horse Rim ($n=18$). Transmitted-light petrography was established on polished sections that were prepared from samples impregnated with blue-stained epoxy resin. These 30-μm-thick sections were stained with alizarin red S and potassium ferricyanide (Dickson, 1966), then examined under plane-polarized light and between crossed-polars using a Nikon Eclipse LV100N POL microscope. These sections were analysed using a CITL Mk5 cold cathodoluminescence (CL) system that is mounted on the microscope (operating conditions = 15 to 20 kV, 350 to 450 μA). Dolomite crystal textures were described according to the nomenclature of Sibley and Gregg (1987).

Five polished sections that include each of the paragenetic stages were analysed for their major and trace element compositions by electron probe micro-analysis (EPMA) using a Cameca SX100. To obtain an overview of each sample, an initial 2 × 10 mm map was created at a stepping-interval of 10 μm. Based on these low-resolution elemental maps, 1.536 × 1.536 mm areas of interest were mapped at a stepping interval of 3 μm. Ca (Kα; PET) and Mg (Kα; TAP) were analysed at 15 kV, 10 nA and a dwell time of 100 ms using calcite and magnesite as standards. Si (Kα; TAP), Fe (Kα; LLIF) and Mn (Kα; LLIF) were analysed at 15 kV, 200 nA, and a dwell time of 200 ms using spessartine, fayalite and tephroite as standards.

These sections were analysed for their rare earth element (REE) concentrations using a Teledyne Photon Machines Analyte Excite+193 nm ArF Excimer laser ablation (LA) system with a HelEx II active 2-volume ablation cell, linked to an Agilent 8900 inductively coupled plasma mass spectrometer (ICP-MS). Ablation of NIST 612 was used to tune the instrument, optimize signal intensities and maintain low levels of oxide formation ($^{232}ThO/^{232}Th < 0.25\%$) and a U/Th ratio that is close to unity. NIST 612 was used as the primary reference material, whereas the JCp-1 NP reference carbonate (Jochum et al., 2019) was treated as a secondary reference. The accuracy of REE measurements on the secondary standard was typically within ±20% of the recommended values for JCp1-NP. Discrepancy was higher for Eu (ca. 40%), which is attributed to uncertainties on reference [Eu] at low abundances (ca. 5 ng g^{-1}). Sample analyses were conducted with a spot diameter of 50 μm, fluence of 3 J cm^{-2} and repetition rate of 5 Hz. Each analysis lasted 40 s and was preceded by 20 s counting time of a gas blank, used to correct signal intensities for background contributions. Data reduction was conducted using the known [Ca] of the reference materials (Jochum et al., 2011, 2019) and the samples (measured by EPMA) in Iolite4 (Paton et al., 2011; Woodhead et al., 2007). Results are reported with their two standard error and detection limit calculated according to Howell et al. (2013).

The $\delta^{13}C$ and $\delta^{18}O$ stable isotopic composition of dolomite ($n=101$) was analysed at the Scottish Universities Environmental Research Centre (SUERC) using an Analytical Precision AP2003 mass spectrometer that is equipped with a separate acid injector system. To isolate each paragenetic stage, samples were micro-drilled (50 μm diameter bit) under a binocular microscope. These ca. 5 mg powders were digested in 105% H_3PO_4 under a helium atmosphere at 70°C. Measured $\delta^{13}C$ and $\delta^{18}O$ values are reported relative to Vienna PeeDee Belemnite (VPDB)

using conventional delta (δ) notation. Analytical reproducibility, based on replicates of the internal standard MAB-2, is ±0.2‰ for $\delta^{13}C$ and $\delta^{18}O$. MAB-2 has the same $\delta^{13}C$ and $\delta^{18}O$ values as the IAEA-CO-1 international standard (−2.5 and 2.4‰ VPDB, respectively).

Carbonate clumped isotope (Δ_{47}) measurements were performed at SUERC using a manual extraction line and a Thermo Fisher 253 mass spectrometer. Samples were digested for 30 min in >103% H_3PO_4 at 90°C in an acid bath. The produced CO_2 was cleaned of contaminants by gas chromatography and the intensities of m/z 44 to 48 were recorded on the mass spectrometer. The signal at m/z 48 was used to screen for contamination following the method described by Davies and John (2017). Data reduction was conducted in Easotope (John & Bowen, 2016), using the IUPAC parameters (Brand et al., 2010; Petersen et al., 2019) and the ^{18}O acid fractionation of Rosenbaum and Sheppard (1986). The values from Bernasconi et al. (2021) for the ETH1 to ETH4 carbonate standards were used to define the empirical transfer function from the measured Δ_{47} to the absolute reference frame. Analytical uncertainties on Δ_{47} were calculated as the larger of the standard error of sample replicates or the standard error of the ETH standards. Crystallization temperatures were calculated from Δ_{47} based on Anderson et al. (2021) and used to calculate $\delta^{18}O_{fluid}$ according to Horita (2014).

An additional eight polished sections were prepared using super glue so that the samples were not heated during their preparation. Following the criteria described by Goldstein and Reynolds (1994), petrographical analyses were conducted to identify primary fluid inclusion assemblages in each paragenetic stage. Fluid inclusion microthermometry was conducted using a Linkam THMS600 heating and freezing stage that is mounted on an Olympus BX53 microscope. The stage temperature was calibrated using synthetic fluid inclusions, according to the triple points of CO_2 (−56.6°C) and H_2O (0°C), and the critical point of H_2O (373.9°C). Measurement accuracy and precision are ±0.5°C at temperatures >100°C. For the smallest inclusions, where phase changes were difficult to observe, the homogenization temperature was bracketed using the temperature cycling approach of Goldstein and Reynolds (1994). The microthermometric data were interpreted quantitatively based on Steele-MacInnis et al. (2012).

4 | FIELD AND PETROGRAPHICAL OBSERVATIONS

4.1 | Field observations

At Whirlpool Point (Figure 2a–c), the lower part of the Cathedral Formation includes (i) thinly bedded (2 to 12 cm), microbial-peloid boundstone and (ii) bioturbated, ooid-peloid mudstone and wackestone (Figure 2d,e). The outcrop is intersected by a fault with a normal offset of 30 cm (Figure 2b). The HTD body is stratabound at its margins (distal to the fault) and non-stratabound at its core (proximal to the fault). The HTD body extends laterally for 85 m in the hangingwall, where it has a sharp, bedding-parallel contact with limestone. The HTD body extends for >140 m in the footwall. Zebra textures (Figure 2f,g) are present up to 70 m from the fault in the hangingwall and up to 120 m in the footwall. Zebra textures are bedding-parallel in the microbial boundstone facies and bedding-inclined in the bioturbated mudstone facies. There is a marked shift whereby the angle of the zebra textures (relative to bedding) increases towards the fault. Dolomite breccias (Figure 2h,i) are present up to 25 m from the fault in the hangingwall and up to 5 m in the footwall. These breccias comprise floating clasts of RD, with highly irregular margins, that are surrounded and apparently suspended in SD. The RD clasts in these breccias include numerous dilatational fractures that are occluded by SD. Based on visual estimates, SD comprises 10% to 30% of the rock volume in zebra textures, whereas it can be up to 60% in dolomite breccias (Figure 2a–c). The bedding-surfaces immediately overlying and adjacent to these rock textures are highly deformed (Figure 2c,h).

At Mistaya Canyon and Num Ti Jah (Figure 3a–d), the Eldon Formation comprises bioturbated ooid-peloid mudstone. Horizontal burrows are common, but the bioturbation intensity of each unit varies significantly. At Mistaya Canyon, a fracture corridor (8 to 12 m wide) intersects the outcrop to the southwest of the road, where the strata are highly eroded. The HTD body is stratabound distal to the fracture corridor and non-stratabound proximal to the fracture corridor. To the northeast of the road, the HTD body is >10 m thick and extends for >300 m as the contacts with limestone are inaccessible. The strata comprise alternating units of RD and SD that either lack zebra textures, or include numerous bedding-inclined zebra textures, respectively (Figure 3a,b). Individual zebra textures have a strikingly constant inclination, but their angles range from 5° to 35° (relative to bedding) within a given locality. At the north end of the outcrop, the strata comprise RD with rare occurrences of SD that are localized in burrows (Figure 3e,f). A striking feature at Mistaya Canyon is the development of two scales of periodicity, namely the centimetre-scale zebra textures and the decimetre- to meter-scale stratabound alternation of clusters of zebra textures (Figure 3b,g). Boxwork textures, with irregular orientations, are located only proximal to the fracture corridor (Figure 3h). At Num Ti Jah, there is no clear evidence of faults that intersect the strata, but there are numerous fractures and zebra textures. Boxwork textures

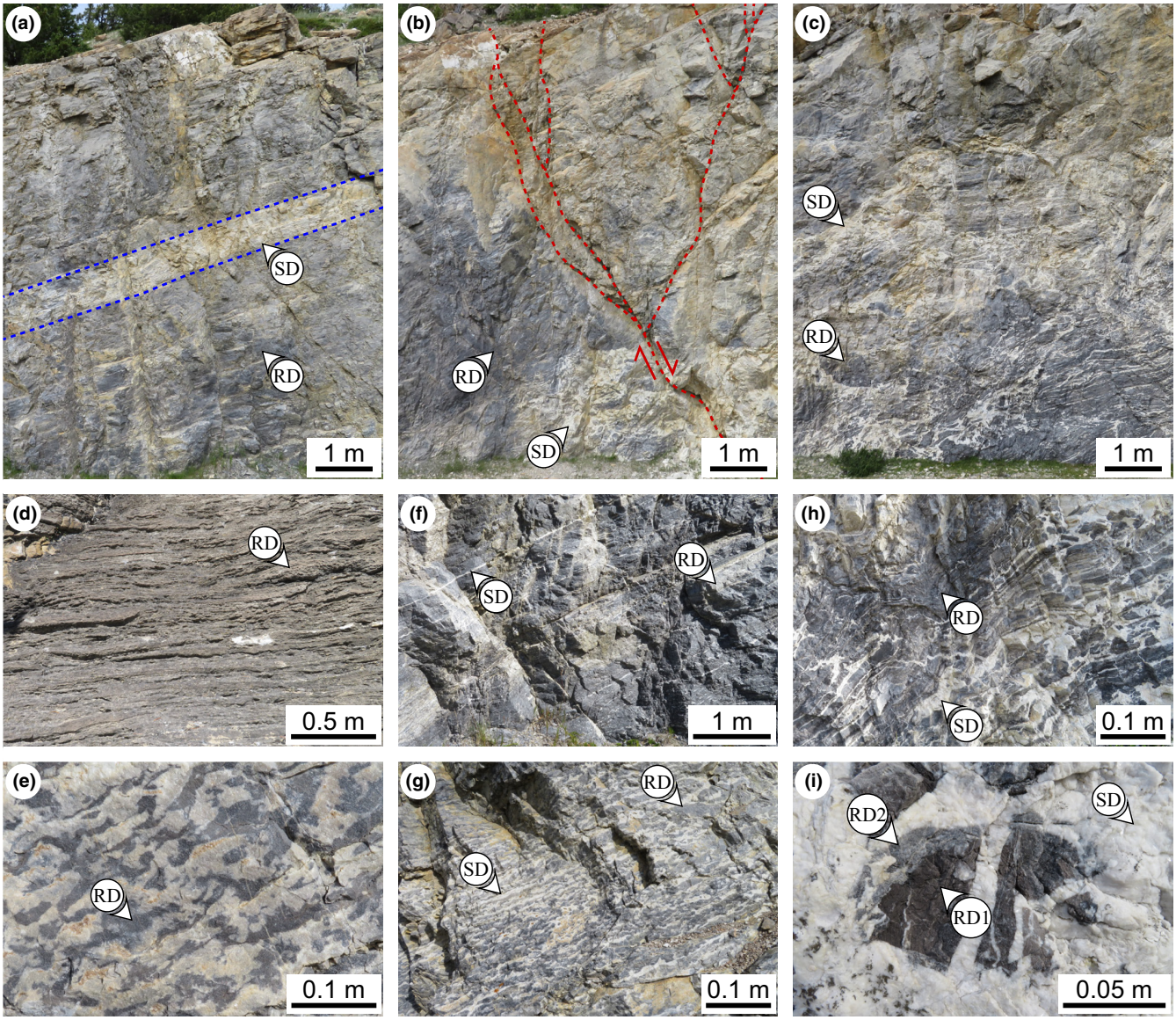

FIGURE 2 Field photographs of the HTD at Whirlpool Point showing the (a) footwall that includes bedding-parallel zebra textures, (b) fault with a normal offset and associated negative flower structure and (c) hangingwall that includes dolomite breccias and bedding-inclined zebra textures. Photographs showing the precursor lithologies, including (d) microbial boundstone and (e) bioturbated peloidal mudstone. Photographs showing the rock textures, including (f,g) Bedding-parallel zebra textures and (h,i) dolomite breccias. RD, replacement dolomite; SD, saddle dolomite.

are located proximal to the contact between the Eldon Formation and the overlying Pika Formation. The quantity of SD also increases towards the contact with the Pika Formation, locally exceeding 60% of the rock volume, yet there is minimal evidence of dilatation of the overlying strata (Figure 3c,d).

At the Kicking Horse Rim (Figure 4a), the upper parts of the Cathedral Formation include (ii) bioturbated, ooid-peloid mudstone and wackestone and (iii) thickly bedded (>10 cm), ooid-pisoid-intraclast wackestone and floatstone. There are several faults, 6 to 8 m in length, with normal offsets of 20 to 80 cm, and numerous fractures distributed throughout the outcrop (Figure 4a). The faults do not propagate through the shale that is interbedded with limestone in the upper 28 m of the Cathedral Formation. Below this shale and limestone, the strata comprise beige, non-stratabound dolomite bodies (sub-vertical to bedding) and grey stratabound dolomite that is present throughout the remainder of the succession. The grey dolomite is similar to the strata described within the platform interior, comprising alternating units of RD and SD with zebra textures that are poorly developed (Figure 4b,c). The beige dolomite comprises units of structureless SD with regions that include numerous bedding-inclined zebra textures (Figure 4d,e). These zebra textures include a faint relict of the original RD, which has highly irregular margins. The

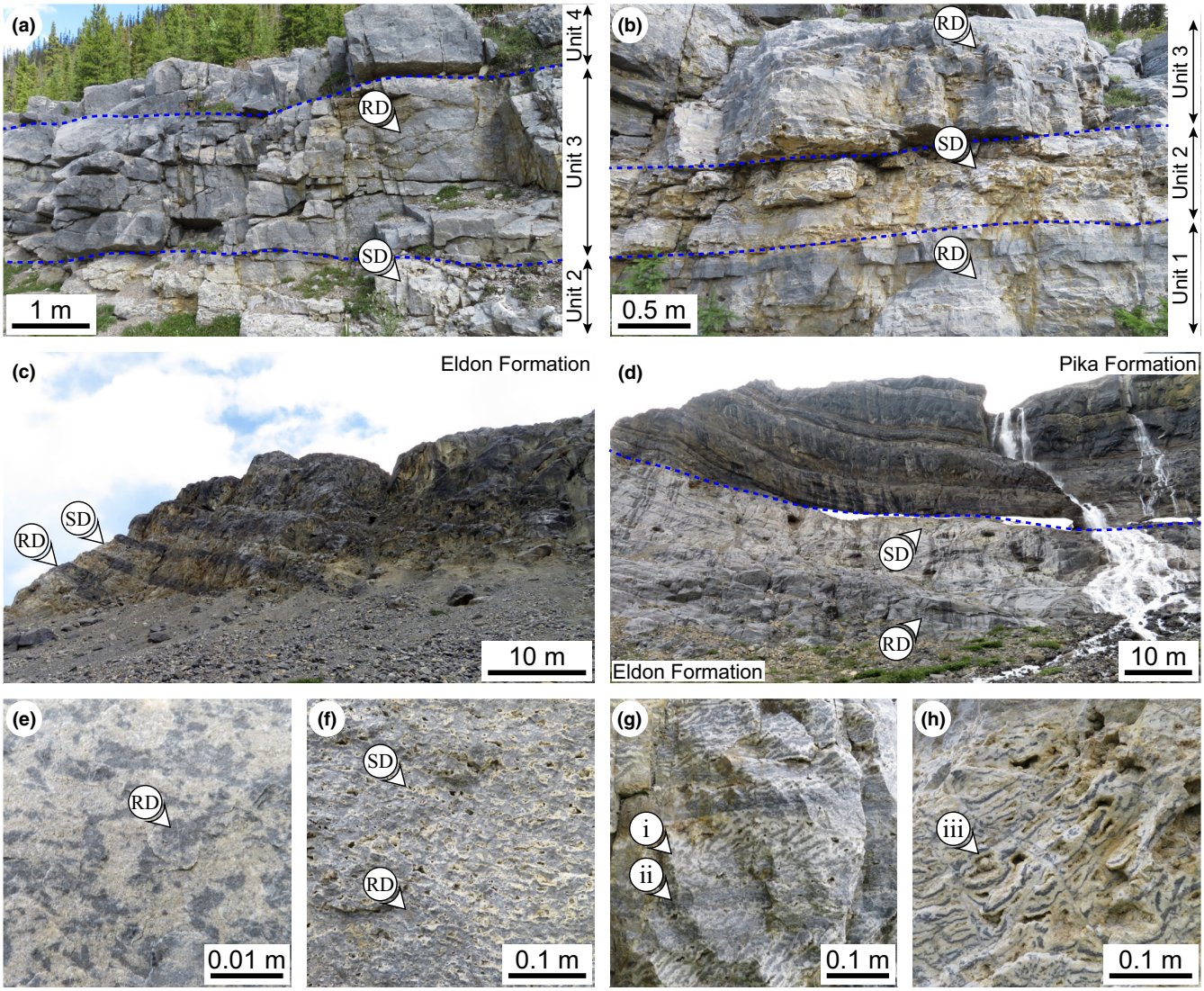

FIGURE 3 (a,b) Field photograph of the HTD at Mistaya Canyon showing the progressive shift from (c) precursor bioturbated mudstone, to (d) nascent zebra textures, to (e) bedding-inclined zebra textures, to (f) boxwork textures. Note that the zebra textures are (i) inclined to bedding, and they (ii) comprise stratabound sets that are constrained to individual beds. (iii) Large vugs, >1.0 cm in diameter, are present throughout the most highly altered units in the exposure. (g,h) Field photograph of the HTD at Num Ti Jah. Note the increase in the abundance of SD proximal to the contact between the Eldon Formation and the Pika Formation. RD, replacement dolomite; SD, saddle dolomite.

zebra textures at the Kicking Horse Rim also include two scales of periodicity, similar to that described at Mistaya Canyon and Num Ti Jah, but there is only a faint relict of the bedding planes that constrain the zebra textures into stratabound sets (Figure 4d). The most striking feature of the succession at the Kicking Horse Rim is that SD commonly exceeds 80% of the rock volume, yet the bedding-surfaces are largely undisturbed and there is minimal evidence of dilatation of the strata (Figure 4a).

4.2 | Petrographical observations

At Whirlpool Point, dolomite breccias are located only proximal to faults, transitioning laterally into zebra textures (Table 1). Zebra textures comprise a series of rock discontinuities, where the grey RD is separated by symmetrical bands of white SD. Adjacent RD bands are negative images of one another and would fit together if the SD bands were removed (Figure 5a,b). These zebra textures are also associated with smaller, mm-scale, en-echelon fractures that are present throughout the RD matrix (Figure 5a). SD crystals are elongate, oriented perpendicular to the zebra textures and meet at a central junction with well-preserved crystal terminations into open pore space. At Whirlpool Point, the zebra textures are typically bedding-parallel, whereas they are bedding-inclined at Mistaya Canyon and Num Ti Jah (Figure 5c,d). Proximal to the contact between the Eldon Formation and the Pika Formation, the RD bands have a beige discoloration,

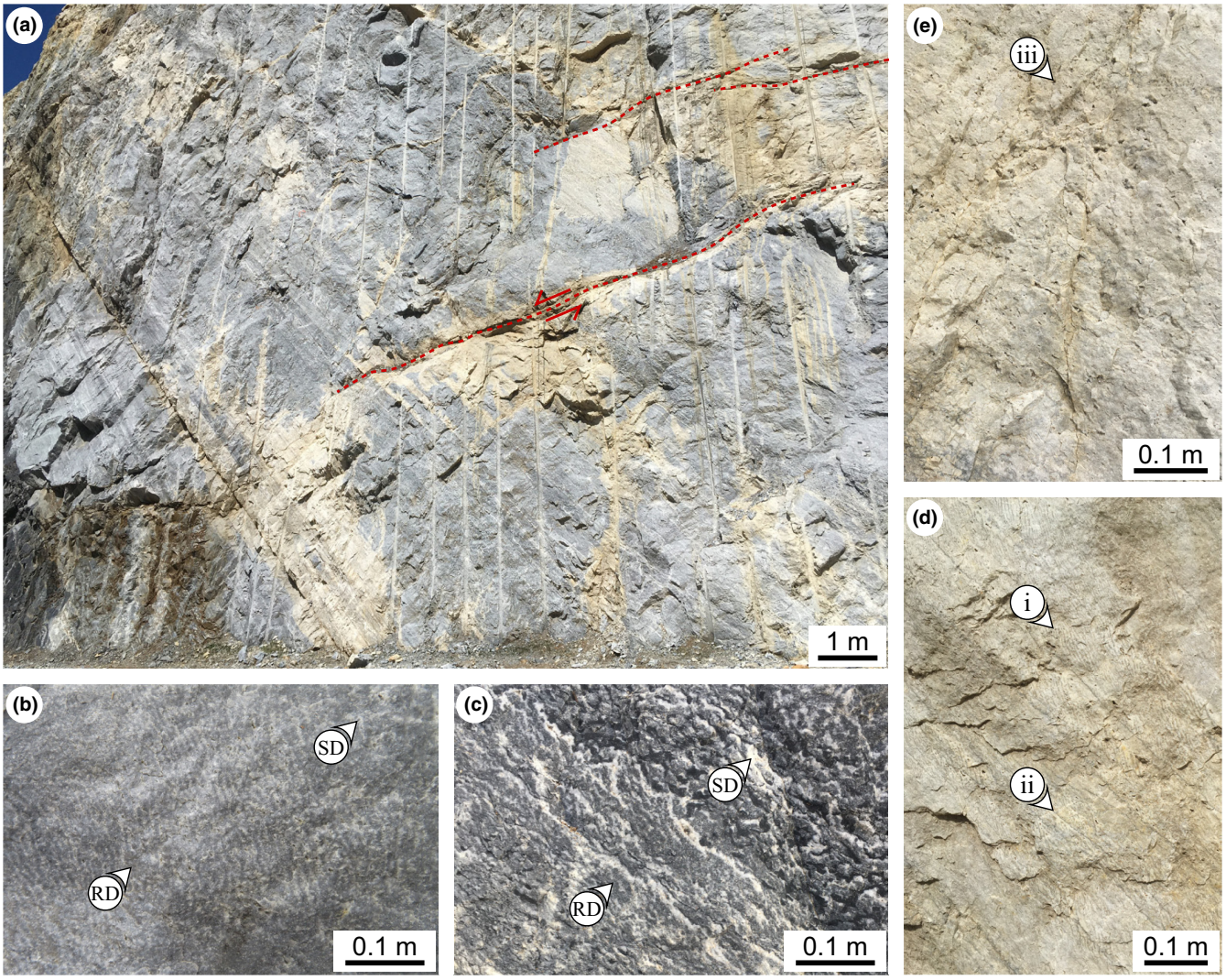

FIGURE 4 (a) Field photograph of the HTD at the Kicking Horse Rim, where zebra textures are present in both the light grey and tan regions of the exposure. (b,c) Nascent zebra textures showing their nucleation and progressive shift into (d,e) highly recrystallized zebra textures and structureless SD. Note that these rock textures are (i) inclined to bedding, and they (ii) comprise stratabound sets that are constrained to individual beds. (iii) Small vugs, <1.0 cm in diameter, are present throughout the most highly altered units in the exposure. RD, replacement dolomite; SD, saddle dolomite.

and they would not fit together if the SD bands were removed (Figure 5e). This discoloration is widespread at the Kicking Horse Rim, where the zebra textures are not aligned with bedding (Figure 5f–i). At the Kicking Horse Rim, the contacts between RD and SD are less distinct, interfingering at the mm-scale, and there is no porosity present between adjacent SD bands (Figure 5g,h).

At Whirlpool Point, the strata include limestone, two phases of RD and three phases of SD (Table 1). RD1 comprises finely crystalline (20 to 150 μm) planar-e dolomite with dull-purple luminescent cores and dull-red luminescent rims, whereas RD2 comprises medium-crystalline (100 to 400 μm) planar-s dolomite with dull-red luminescent cores and dull- to medium-red luminescent rims (Figure 6a). RD1 includes clay minerals, detrital quartz and organic matter that are rare in RD2. RD2 is unzoned proximal to the fault. SD1 (250 to 4500 μm) comprises unzoned, dull- to medium-red luminescent, non-planar dolomite that form a syntaxial layer nucleated on RD2. The crystals in SD1 gradually becoming coarser towards the center of the zebra texture (Figure 6b). SD2 comprises nonplanar dolomite, with a characteristic dull- to bright- red and orange oscillatory zonation, that form rims (250 to 1250 μm thick) nucleated on SD1 crystals (Figure 6c). There are no clay minerals or quartz in SD1 or SD2.

At Mistaya Canyon and Num Ti Jah, the petrographical phases are analogous to those described at Whirlpool Point, but limestone is absent (Table 1). Stylolites are common and, in many cases, form the boundary between RD1 and RD2. Microfractures, with apertures that are <100 μm, are oriented perpendicular

TABLE 1 Summary table describing the geometries of the hydrothermal dolomite (HTD) bodies, predominant rock textures and microscopic characteristics of each of the paragenetic stages in the Cathedral Formation and the Eldon Formation (Middle Cambrian, WCSB).

Locality	Geometries of the HTD bodies	Predominant rock textures	Paragenetic stage	Dolomite texture	Cathodoluminescence	Other features
Whirlpool Point (Cathedral Formation)	Stratabound distal to faults, non-stratabound proximal to faults. Increased abundance of saddle dolomite in the hanging-wall of faults	Bedding-parallel zebra textures. Dolomite breccias located in the central ca. 30 m of the HTD body	RD1	Planar-e to planar-s	Concentric zoning, dull-purple cores, dull-red rims	Fabric-retentive, detrital quartz and organic matter locally common
			RD2	Planar-s to nonplanar-a	Blotchy zoning, dull-red cores, dull-red to medium-red rims	Fabric-destructive, locally associated with stylolites. Detrital quartz rare
			SD1	Nonplanar (saddle)	Unzoned, dull-red to medium-red	Form syntaxial layers on RD2. Elongate crystals normal to cavity wall
			SD2	Nonplanar (saddle)	Oscillatory zoning, dull-red to bright-red and dull-orange to bright-orange	Breccia and fracture fill, commonly form rims nucleated on SD1. Pb-Zn-Fe sulphides locally common
Mistaya Canyon and Num Ti Jah (Eldon Formation)	Largely stratabound, locally non-stratabound proximal to faults and proximal to the upper contact with the Pika Formation	Bedding-inclined zebra textures in stratabound units. Boxwork textures locally common proximal to faults and fractures	RD1	Planar-e to planar-s	Concentric zoning, medium-purple and medium-red cores, dull-red rims	Fabric-retentive, detrital quartz and organic matter locally common
			RD2	Planar-s to nonplanar-a	Blotchy zoning to unzoned, medium-red cores, medium-red rims	Fabric-destructive, locally associated with stylolites. Detrital quartz rare
			SD1	Nonplanar (saddle)	Unzoned, dull-red to medium-red	Form syntaxial layers on RD2. Elongate crystals normal to cavity wall
			SD2	Nonplanar (saddle)	Oscillatory zoning, dull-red to bright-red and dull-orange to bright-orange	Breccia and fracture fill, commonly form rims nucleated on SD1. Pb-Zn-Fe sulphides locally common
Kicking Horse Rim (Cathedral Formation)	Non-stratabound, irregular patterns	Numerous bedding-inclined zebra textures with scattered patches of structureless saddle dolomite. Rare bedding-parallel zebra textures	RD2	Nonplanar-a	Unzoned, dull-red to medium-red, irregular patterns	Fabric-destructive, stylolites common, irregular crystal boundaries. Pb-Zn-Fe sulphides locally common
			SD1	Nonplanar (saddle)	Unzoned, dull-red to medium-red	Form syntaxial layers on RD2. Elongate crystals normal to cavity wall. Pb-Zn-Fe sulphides locally common
			SD2	Nonplanar (saddle)	Oscillatory zoning, dull-red to bright-red and dull-orange to bright-orange	Breccia and fracture fill, commonly form rims nucleated on SD1. Pb-Zn-Fe sulphides locally common

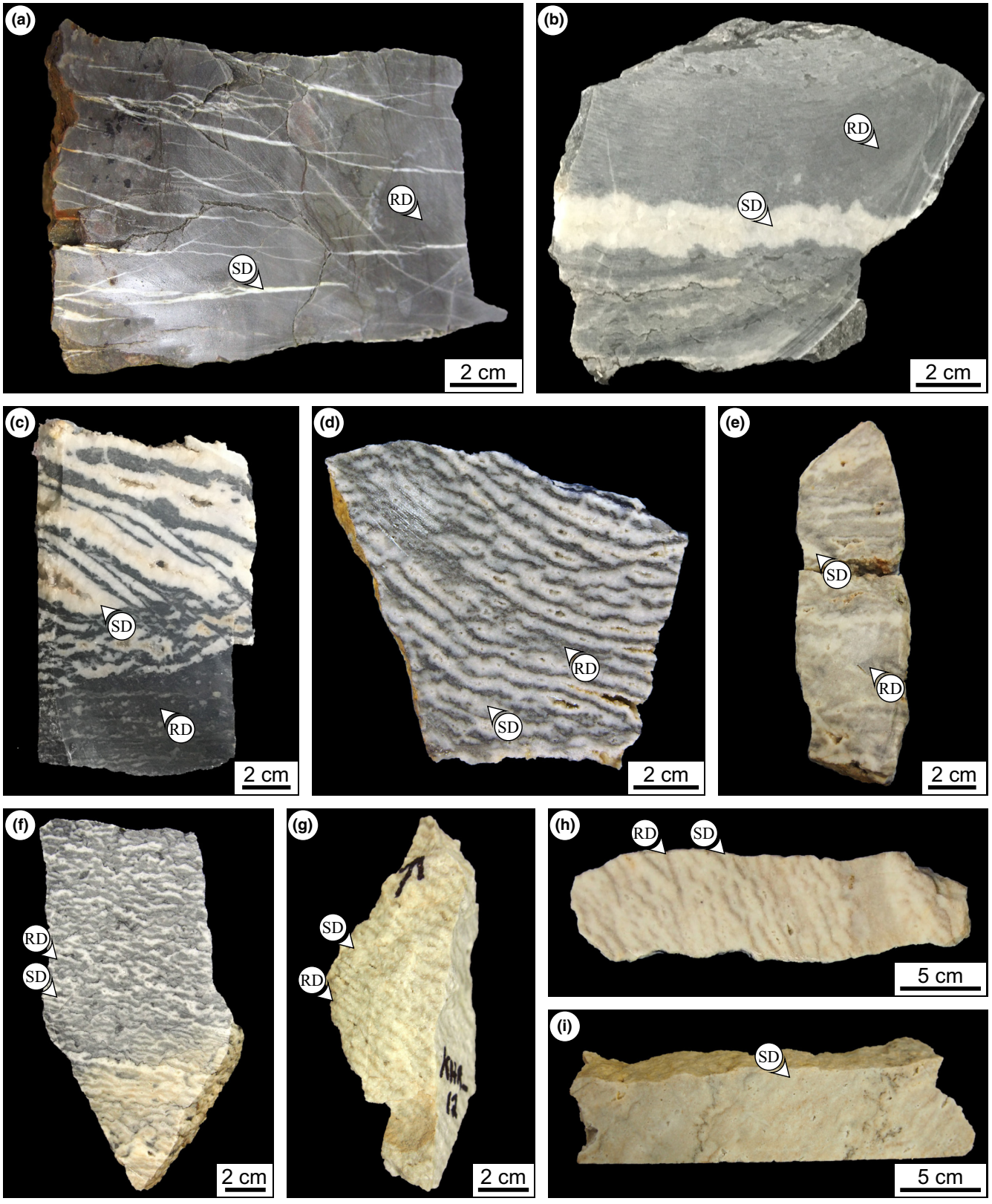

FIGURE 5 Hand sample photographs showing the petrographical characteristics of the zebra textures in (a,b) the Cathedral Formation at Whirlpool Point, (c–e) the Eldon Formation at Mistaya Canyon and Num Ti Jah and (f–i) the Cathedral Formation at the Kicking Horse Rim. Note that the zebra textures are symmetrical, with opposing walls that are negative images of one another at Whirlpool Point (platform interior), whereas the zebra textures have irregular margins, interfingering at the mm-scale, at the Kicking Horse Rim (platform margin). RD, replacement dolomite; SD, saddle dolomite.

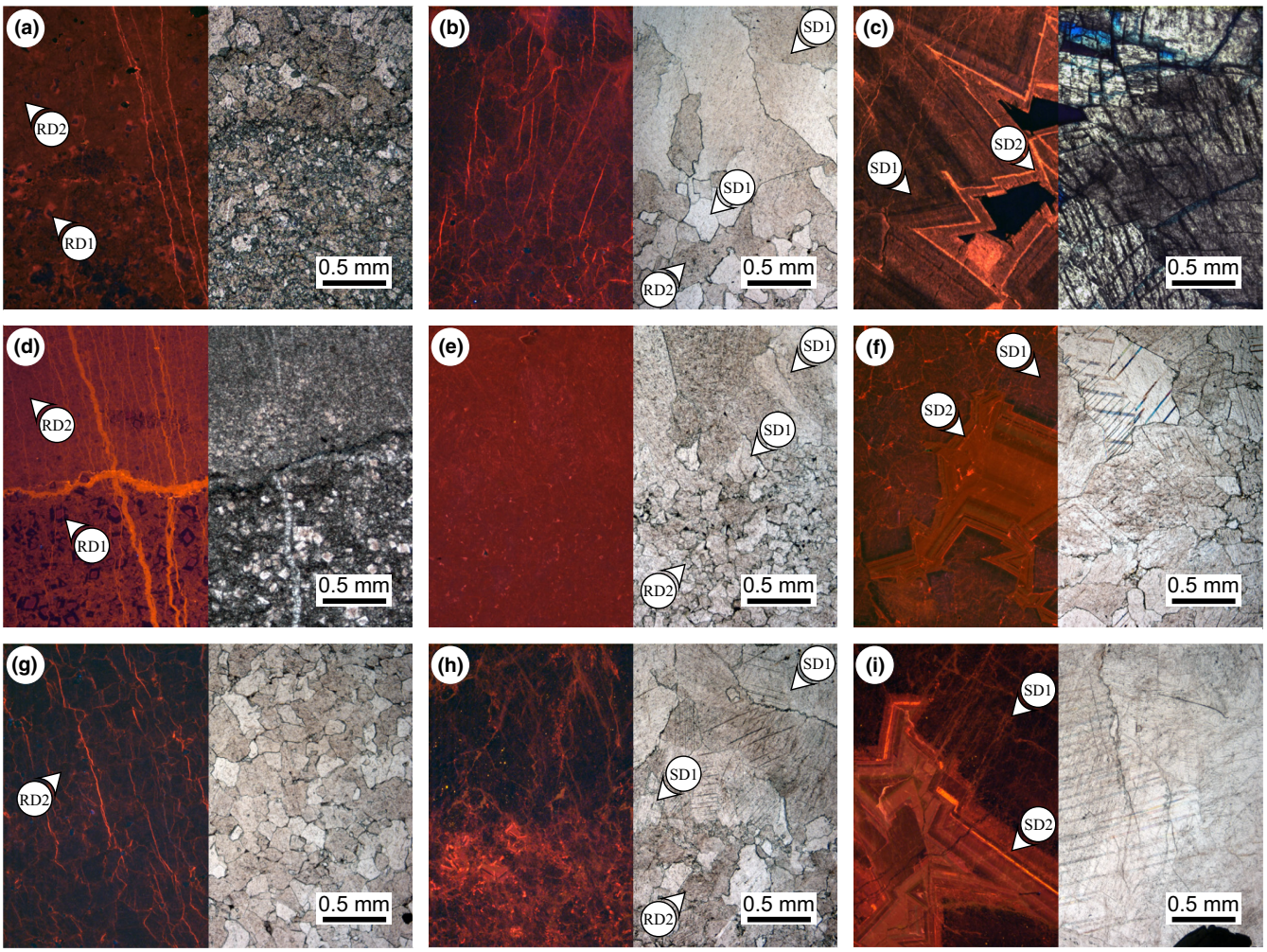

FIGURE 6 Cathodoluminescence (CL; left) and transmitted light (TL; right) photomicrographs showing the different phases of dolomite that are present in (a–c) the Cathedral Formation at Whirlpool Point, (d–f) the Eldon Formation at Mistaya Canyon and Num Ti Jah and (g–i) the Cathedral Formation at the Kicking Horse Rim. Note that RD1 is not present at the Kicking Horse Rim and that SD2 increases in abundance from Whirlpool Point to the Kicking Horse Rim. RD, replacement dolomite; SD, saddle dolomite.

to these stylolites (Figure 6d). The CL characteristics of RD2 and SD1 are homogenous, but these phases can be differentiated in transmitted light due to the contrast in the abundance of clay minerals and detrital quartz across this contact (Figure 6e). Relative to the Cathedral Formation, SD2 is less abundant in the Eldon Formation and has notably duller CL characteristics (Figure 6f). At the Kicking Horse Rim, RD1 is not present and RD2 comprises medium-crystalline, nonplanar dolomite with a dull- to moderate-red luminescence (Table 1; Figure 6g). Proximal to the zebra textures, RD2 has a bright-red luminescence, with highly irregular margins and local crystal size reduction along the contact between RD2 and SD1 (Figure 6h). At the Kicking Horse Rim, RD2 has textural characteristics (unzoned, irregular margins) that are similar to RD2 in locations that are proximal to faults at Whirlpool Point. SD2 is also significantly more abundant at the Kicking Horse Rim than at Whirlpool Point, and its CL characteristics are notably brighter (Figure 6i).

5 | GEOCHEMICAL RESULTS

5.1 | Major and trace element analyses

Selected results from EPMA are summarized in Table 2. RD1, RD2 and SD1 comprise near-stoichiometric dolomite, with %Ca (molar Ca/[Ca+Mg]) values that range from 47.8% to 51.4%. %Ca values in SD2 (47.2% to 51.6%) have a wider range than these earlier paragenetic stages. In the platform interior, %Ca values are relatively constant at Whirlpool Point (49.8% to 50.5%), Mistaya Canyon (50.9% to 51.6%) and Num Ti Jah (49.6% to 50.1%) but then significantly decrease towards the platform margin at the Kicking Horse Rim (47.2% to 48.2%). Due to the presence

of detrital quartz between the dolomite crystals, [Si] is markedly higher in the RD relative to the SD, but the [Si] within the dolomite crystals is typically <100 ppm and, thus, below the resolution required to systematically investigate these trends (Table 2).

Visualization of μm-scale geochemical variations is facilitated by high [Fe], which covaries linearly with [Mn] (correlation coefficient >.95; Table 2). The [Fe] and [Mn] are notably higher in the Cathedral Formation (Figure 7a,d) relative to the Eldon Formation (Figure 7b,c), and there is an increasing trend from Whirlpool Point ([Fe] = 2407 to 12,130 ppm, [Mn] = 183 to 1190 ppm) to the Kicking Horse Rim ([Fe] = 6890 to 14,300 ppm, [Mn] = 1140 to 2180 ppm). In the platform interior, these trace element concentrations are highly differentiated and SD2 has a marked enrichment of Fe and Mn relative to RD1, RD2 and SD1 (Figure 7a–c). In contrast, Fe and Mn are much more homogenous at the platform margin (Figure 7d). Based on its CL characteristics (oscillatory zoned, dull- to bright- red), the final paragenetic stage at the Kicking Horse Rim was assigned to SD2, but this phase has an enigmatic decrease in [Fe] and [Mn] that it is accompanied by an increase in [Mg] (Table 2). Therefore, it should be noted that magnesite has been reported in the vicinity of the Kicking Horse Rim (Paradis & Simandl, 2017; Powell et al., 2006; Vandeginste et al., 2007).

5.2 | Rare earth element analyses

Rare earth element and yttrium (REE + Y) concentrations are shown in Figure 8, with the light (∑LREE), middle (∑MREE) and heavy (∑HREE) REE values summarized in Table 2. At Whirlpool Point, limestone has consistent ∑LREE (0.063 ppm), ∑MREE (0.076 ppm) and ∑HREE (0.069 ppm). RD1 has a similar REE profile as limestone, but with enriched ∑LREE (0.11 ppm), ∑MREE (0.19 ppm) and ∑HREE (0.11 ppm). RD2 and SD1 have different REE profiles than limestone, with characteristic ∑MREE enrichment relative to their ∑LREE. This shift is distinct in SD2, which has enriched ∑MREE (0.46 ppm) and ∑HREE (0.23 ppm) relative to its ∑LREE (0.049 ppm). Such depleted ∑LREE are also characteristic of SD2 at Mistaya Canyon, Num Ti Jah and the Kicking Horse Rim. Overall, the [REE] are higher in the Cathedral Formation relative to the Eldon Formation. RD1, RD2 and SD1 are also less differentiated at Mistaya Canyon and Num Ti Jah, plotting in a tight cluster (Figure 8b,c). At the Kicking Horse Rim, RD2 and SD2 have similar [REE] as their respective paragenetic stages at Whirlpool Point. Conversely, SD2 is markedly enriched in ∑LREE (0.17 ppm), ∑MREE (0.91 ppm) and ∑HREE (0.35 ppm) at the Kicking Horse Rim (Figure 8d).

Calculated Ce anomalies ($Ce/Ce^* = [Ce]/[0.5La+0.5Pr]$), Pr anomalies ($Pr/Pr^* = [Pr]/[0.5Ce+0.5Nd]$) and Eu anomalies ($Eu/Eu^* = Eu/[0.67Sm+0.33Tb]$) are shown in Table 2. Values >1.0 are deemed positive, whereas values <1.0 are considered negative anomalies. At Whirlpool Point, limestone has a prominent negative Ce/Ce* (0.80) and a positive Pr/Pr* (1.1). With each later paragenetic stage (e.g. RD1, RD2, SD1), the Ce/Ce* systematically increases and the Pr/Pr* decreases (Figure 8e; Table 2). At Mistaya Canyon and Num Ti Jah, the Ce/Ce* and the Pr/Pr* of RD1, RD2 and SD1 plot in a narrow range that is close to 1.0 (Figure 8e; Table 2). Conversely, RD2 and SD1 have positive Ce/Ce* (1.1) and negative Pr/Pr* (0.95) at the Kicking Horse Rim (Figure 8e). At each locality, SD2 plots separately from these earlier paragenetic stages, with negative Ce/Ce* and Pr/Pr* (Figure 8e; Table 2). Such a relationship is also evident when the Eu/Eu* is plotted against ΣMREE/ΣLREE, where the values for SD2 are markedly higher than RD1, RD2 and SD1 (Figure 8f; Table 2).

5.3 | Stable and clumped isotope analyses

Mean carbon and oxygen stable isotope ratios ($\delta^{13}C_{VPDB}$, $\delta^{18}O_{VPBD}$) and their standard deviations are plotted in Figure 9a, with values shown in Table 2. At Whirlpool Point, mean $\delta^{13}C$ and $\delta^{18}O$ in limestone are −0.7‰ and −11.5‰, respectively. Relative to limestone, each of the later paragenetic stages at Whirlpool Point are increasingly more depleted in $\delta^{13}C$ and $\delta^{18}O$ (RD1 = −0.6‰, −11.7‰; RD2 = −0.7‰, −12.5‰; SD1 = −0.7‰, −13.1‰; SD2 = –0.8‰, −14.1‰). Relative to Whirlpool Point, the mean $\delta^{13}C$ and $\delta^{18}O$ of the dolomite at Mistaya Canyon and Num Ti Jah are more depleted (−0.9 to −1.1‰, −14.2 to −15.8‰), and this trend continues towards the Kicking Horse Rim, where the mean $\delta^{13}C$ and $\delta^{18}O$ of the dolomite are the most depleted in the study area (−1.0 to −1.3‰, −17.0 to −19.8‰).

Clumped isotope (Δ_{47}) values are shown in Table 2, with their respective crystallization temperatures ($T\Delta_{47}$; calculated from Anderson et al., 2021) plotted in Figure 9b. At Whirlpool Point, Δ_{47} values range from 0.362 to 0.371‰, which corresponds to $T\Delta_{47}$ of 150 to 159°C. At each locality, paragenetic variations are typically within the error margin of each adjacent phase (Figure 9b). Δ_{47} values decrease at Mistaya Canyon and Num Ti Jah (0.322 to 0.343‰), which corresponds to $T\Delta_{47}$ of 180 to 207°C. This trend continues towards the Kicking Horse Rim, where the Δ_{47} values are 0.258 to 0.274‰ and the $T\Delta_{47}$ are 294 to 336°C. Based on these $\delta^{18}O$ and $T\Delta_{47}$ values, $\delta^{18}O_{fluid}$ was calculated according to Horita (2014) and shown in Table 2 (reported in SMOW). $\delta^{18}O_{fluid}$ values increase from Whirlpool Point (2.8 to 4.6‰), to Mistaya Canyon and Num Ti Jah (2.9 to 5.4‰), to the Kicking Horse Rim (4.5 to 7.0‰).

TABLE 2 Selected major, trace and rare earth element concentrations, as well as the results from stable and clumped isotope, and fluid inclusion analyses on the Cathedral Formation and the Eldon Formation (Middle Cambrian, WCSB).

Locality	Phase		Ca (wt%)	Mg (wt%)	Si (wt%)	Fe (ppm)	Mn (ppm)	∑LREE (ppm)	∑MREE (ppm)	∑HREE (ppm)
Whirlpool Point (Cathedral Formation)	Lst.	Mean	–	–	–	–	–	0.063	0.076	0.069
		Std. dev.	–	–	–	–	–	0.006	0.007	0.010
	RD1	Mean	20.82	12.52	1.62[a]	2407	183	0.111	0.186	0.109
		Std. dev.	2.23	1.78	5.01[a]	2098	213	0.045	0.175	0.051
	RD2	Mean	21.10	12.91	0.94[a]	4907	340	0.122	0.294	0.132
		Std. dev.	2.20	1.74	3.65[a]	3650	218	0.059	0.144	0.078
	SD1	Mean	21.13	12.92	0.01	2740	335	0.055	0.137	0.090
		Std. dev.	2.21	1.75	0.49	1505	160	0.038	0.152	0.059
	SD2	Mean	20.45	12.14	0.02	12,130	1190	0.049	0.462	0.232
		Std. dev.	2.26	1.82	0.09	2030	660	0.034	0.183	0.111
Mistaya Canyon (Eldon Formation)	RD1	Mean	22.21	12.75	0.22[a]	1010	164	0.057	0.088	0.047
		Std. dev.	2.21	1.36	1.31[a]	701	112	0.004	0.008	0.002
	RD2	Mean	22.13	12.85	0.13[a]	1290	215	0.066	0.103	0.055
		Std. dev.	2.33	1.44	1.19[a]	740	229	0.007	0.012	0.003
	SD1	Mean	22.15	12.94	0.01	1190	198	0.031	0.047	0.025
		Std. dev.	2.08	1.32	0.11	850	213	0.008	0.016	0.006
	SD2	Mean	20.91	11.90	0.01	8880	1135	0.066	0.490	0.129
		Std. dev.	3.89	2.36	0.19	2280	510	0.021	0.202	0.058
Num Ti Jah (Eldon Formation)	RD1	Mean	22.68	13.71	0.15[a]	984	176	0.019	0.036	0.031
		Std. dev.	2.33	1.63	1.02[a]	721	156	0.002	0.005	0.005
	RD2	Mean	22.49	13.79	0.10[a]	1280	213	0.021	0.038	0.033
		Std. dev.	2.29	1.41	0.98[a]	1180	197	0.003	0.007	0.007
	SD1	Mean	22.61	13.93	0.01	1030	172	0.017	0.032	0.028
		Std. dev.	2.87	1.92	0.12	910	168	0.002	0.008	0.007
	SD2	Mean	21.69	13.20	0.01	5525	789	0.028	0.169	0.098
		Std. dev.	4.28	2.89	0.14	3205	355	0.011	0.091	0.060
Kicking Horse Rim (Cathedral Formation)	RD2	Mean	21.50	13.99	0.46[a]	11,875	1935	0.112	0.177	0.128
		Std. dev.	2.58	1.35	2.31[a]	5735	885	0.036	0.085	0.060
	SD1	Mean	21.66	14.37	0.01	14,300	2180	0.065	0.109	0.082
		Std. dev.	2.31	1.74	0.13	3900	810	0.018	0.045	0.027
	SD2	Mean	21.69	14.69	0.01	6890	1140	0.171	0.905	0.347
		Std. dev.	2.39	1.81	0.16	2580	450	0.120	0.899	0.324

Note: $T\Delta_{47}$ values were calculated from Anderson et al. (2021), whereas $\delta^{18}O_{fluid}$ values were calculated from Horita (2014).

[a]Note that the high [Si] in RD1 and RD2 are influenced by detrital quartz grains that are present between dolomite crystals.

5.4 | Fluid inclusion analyses

Fluid inclusions in RD1 and RD2 are sparse, diminutive (2 to 6 μm in diameter), and assemblages were not observed. Thus, several isolated inclusions hosted in the same crystal were analysed to test for consistency. The inclusions in SD1 and SD2 are 4 to 12 μm in diameter and form primary assemblages within individual crystallographic growth zones. The inclusions analysed were two-phase, liquid+vapour inclusions (ca. 80% liquid, ca. 20% vapour by volume). RD1, RD2 and SD1 also host numerous dark inclusions that appear to contain only a single-phase fluid at room temperature. Conversely, SD2 is limpid and lacks single-phase inclusions. Fluid inclusion homogenization temperatures (T_h) are plotted in Figure 9c, with the values shown in Table 2. T_h values range from 138 to 151°C at Whirlpool Point, 164 to 179°C at Mistaya Canyon and Num Ti Jah, and 182 to 192°C at the Kicking Horse Rim. Melting temperature (T_m) measurements of the fluid inclusions were attempted, but the inclusions could not be frozen during these analyses, even after cooling down to −175°C.

Ce/Ce*	Pr/Pr*	Eu/Eu*	$\delta^{13}C$ (‰, VPDB)	$\delta^{18}O$ (‰, VPDB)	Δ_{47} (‰; CDES)	$T\Delta_{47}$ (°C)	$\delta^{18}O_{fluid}$ (‰, SMOW)	T_h (°C)
0.796	1.111	1.165	−0.68	−11.48	–	–	–	–
0.015	0.020	0.034	0.03	0.49	–	–	–	–
0.852	1.070	1.223	−0.59	−11.73	0.3711	150	4.6	138
0.099	0.068	0.073	0.15	0.47	0.0101	10.2	–	5.6
0.885	1.033	1.271	−0.70	−12.49	0.3628	158	4.5	139
0.127	0.045	0.492	0.19	0.96	0.0023	12.3	–	5.0
0.995	1.013	1.285	−0.73	−13.14	0.3619	159	3.9	141
0.062	0.060	0.216	0.11	0.44	0.0160	10.0	–	5.7
0.818	0.916	1.547	−0.78	−14.12	0.3638	157	2.8	151
0.131	0.073	0.469	0.05	0.86	0.0174	13.1	–	4.8
0.984	1.040	1.250	−0.91	−14.25	0.3434	180	4.3	167
0.048	0.047	0.174	0.24	1.12	0.0233	16.9	–	4.2
0.994	1.051	1.203	−1.03	−15.13	0.3242	204	4.9	176
0.063	0.061	0.226	0.20	0.92	0.0306	26.7	–	5.4
0.955	1.001	1.496	−1.03	−15.51	0.3359	189	3.6	164
0.066	0.042	0.248	0.28	1.13	0.0222	17.1	–	6.0
0.908	0.861	1.645	−1.06	−15.84	0.3402	183	2.9	175
0.548	0.104	0.566	0.12	1.44	0.0086	10.2	–	6.3
0.931	0.958	1.241	−0.93	−14.82	0.3225	207	5.4	179
0.030	0.092	0.303	0.07	0.48	0.0234	20.3	–	4.9
0.928	0.945	1.246	−0.97	−15.36	0.3283	199	4.4	177
0.042	0.113	0.430	0.07	0.57	0.0139	11.6	–	4.5
0.969	0.981	1.176	−0.99	−15.45	0.3346	190	3.8	164
0.077	0.105	0.460	0.10	0.72	0.0131	11.0	–	6.1
0.883	0.919	1.592	−0.95	−15.53	0.3382	186	3.4	177
0.102	0.109	0.741	0.10	0.99	0.0095	10.6	–	5.4
1.066	0.935	1.193	−0.97	−17.05	0.2742	294	7.0	182
0.045	0.038	0.179	0.31	1.64	0.0163	27.6	–	4.7
1.063	0.947	1.146	−1.08	−19.17	0.2582	336	6.2	186
0.047	0.060	0.244	0.30	0.82	0.0106	25.5	–	6.8
0.879	0.954	1.626	−1.26	−19.83	0.2714	301	4.5	192
0.138	0.179	0.718	0.05	0.32	0.0078	26.3	–	6.2

6 | INTERPRETATIONS

6.1 | Timing and depth of dolomitization

The HTD bodies that are hosted in the Cathedral Formation and the Eldon Formation have been variously interpreted to have formed in both compressional and extensional tectonic settings. Symons et al. (1998) suggested that dolomitization occurred during the Laramide Orogeny (Cretaceous to Palaeocene), whereas Vandeginste et al. (2005) suggested that it occurred during the Antler Orogeny (Devonian to Mississippian). Absolute age dating of dolomite, however, has not yet been consistently achieved. Vandeginste et al. (2005), for example, used K-Ar dating on a muscovite phase that post-dates the dolomite to suggest that dolomitization occurred prior to 338 Ma. Conversely, Stacey et al. (2021) interpreted that dolomitization to have occurred soon after deposition, at shallow depths, because RD is crosscut by low-amplitude, bedding-parallel stylolites (Figure 10a,b). This suggests that dolomitization occurred under extensional tectonic

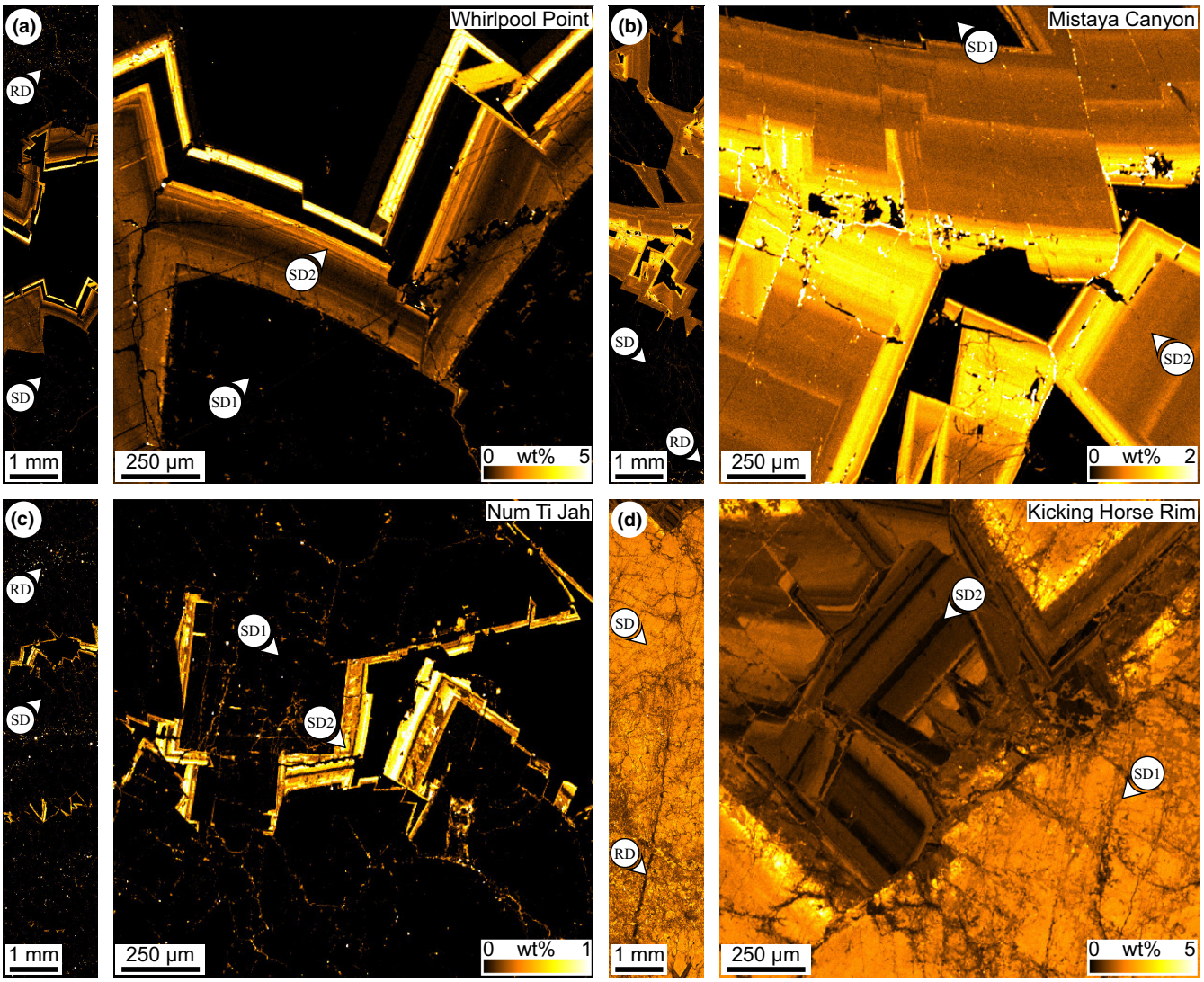

FIGURE 7 Low-resolution (left; 10 µm stepping-interval) and high-resolution (right; 3 µm stepping-interval) electron probe micro-analysis (EPMA) maps showing the spatial distribution of Fe in each of the paragenetic stages at (a) Whirlpool Point, (b) Mistaya Canyon, (c) Num Ti Jah and (d) the Kicking Horse Rim. 1.0 wt% = 10,000 ppm.

conditions (late syn-rift to early post-rift) during the middle to late Cambrian (Koeshidayatullah et al., 2020; Stacey et al., 2021). Further support for this model is provided by identification of a dolomitized megabreccia in the basinal equivalent of the Cathedral Formation, which would indicate dolomitization prior to and during the deposition of the Stephen Formation (Collom et al., 2009; Johnston et al., 2009; Powell et al., 2006). These interpretations are similar to those of Shelton et al. (2019) for the Dublin Basin, Ireland, where reworked clasts of zebra textures in Viséan carbonates were re-deposited in a younger, Viséan debrite. Without age constraints on each paragenetic stage, however, the timing of cementation and recrystallization in the WCSB is equivocal.

6.2 | Textural interpretation of the rock textures in hydrothermal dolomite bodies

Middle Cambrian strata in the WCSB include two phases of RD and three phases of SD (Figure 10a,b). RD is interpreted to have formed through replacement dolomitization due to the fabric-retentive preservation of sedimentological textures, allochems and detrital quartz (Figure 2d,e; Table 2). This interpretation is consistent with numerous works which have shown that the grey, finely crystalline bands formed by replacement (Krebs & Macqueen, 1984; Morrow, 2014; Wallace et al., 1994). At Whirlpool Point, Stacey et al. (2021) suggested that replacement dolomitization occurred during the Cambrian, prior to significant burial, because individual crystals are

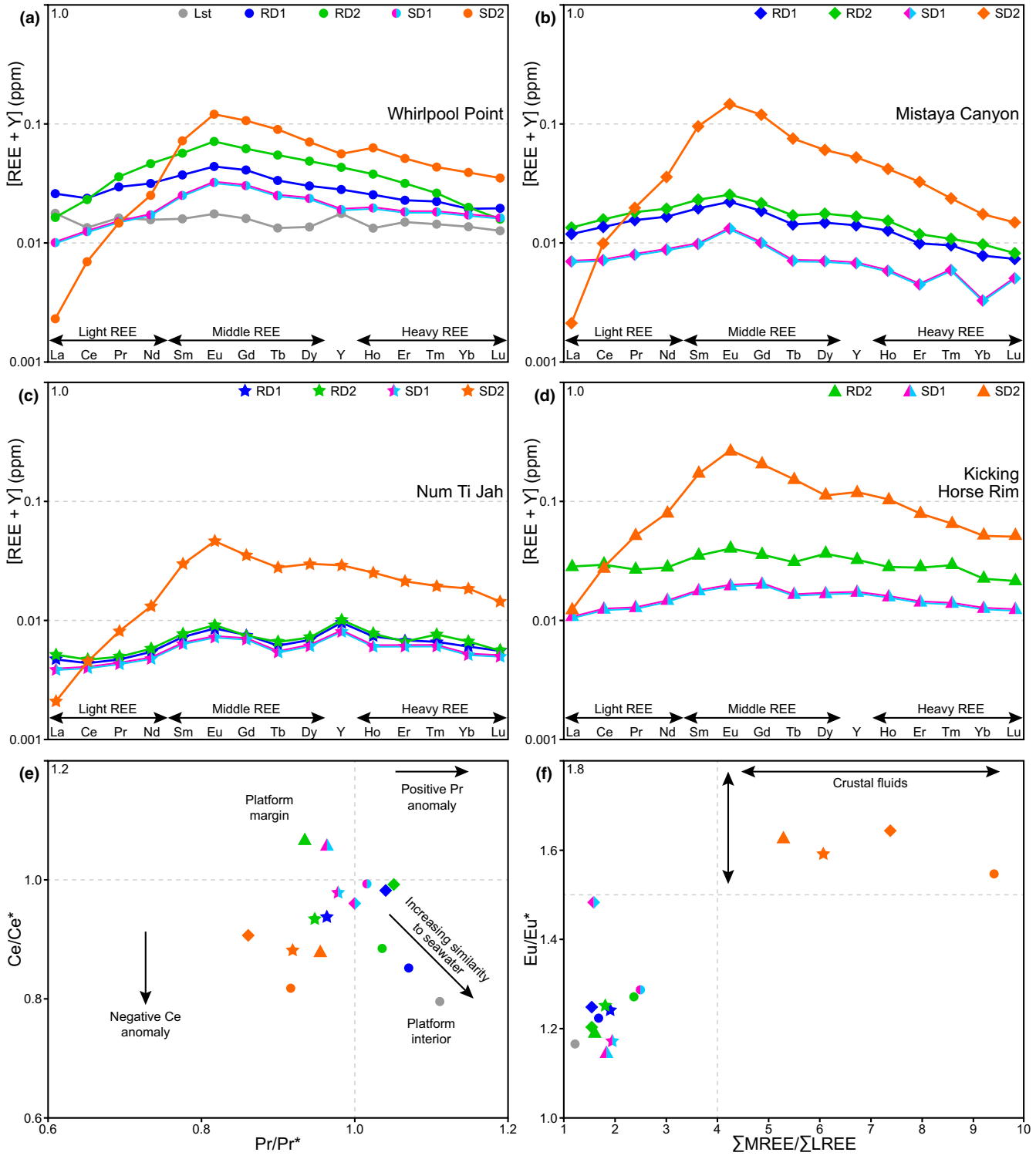

FIGURE 8 Post Archaean Australian Shale (PAAS) normalized (Nance & Taylor, 1976; Taylor & McLennan, 1985) rare earth element (REE) and yttrium (Y) concentrations in each of the paragenetic stages at (a) Whirlpool Point, (b) Mistaya Canyon, (c) Num Ti Jah and (d) the Kicking Horse Rim. (e) Ce/Ce* vs. Pr/Pr* plot showing the decrease in the contribution of seawater from the platform interior to the platform margin. (f) Eu/Eu* versus ΣMREE/ΣLREE plot that illustrates the marked change in composition that occurs in SD2. Lst, limestone; RD, replacement dolomite; SD, saddle dolomite.

crosscut by low-amplitude, bedding-parallel stylolites (cf. Martín-Martín et al., 2018). Conversely, there are no sedimentological textures, allochems or detrital quartz in SD (Figures 2i and 3h; Table 2). Wallace and Hood (2018) outline the petrographical features which demonstrate that the light, coarsely crystalline bands formed by

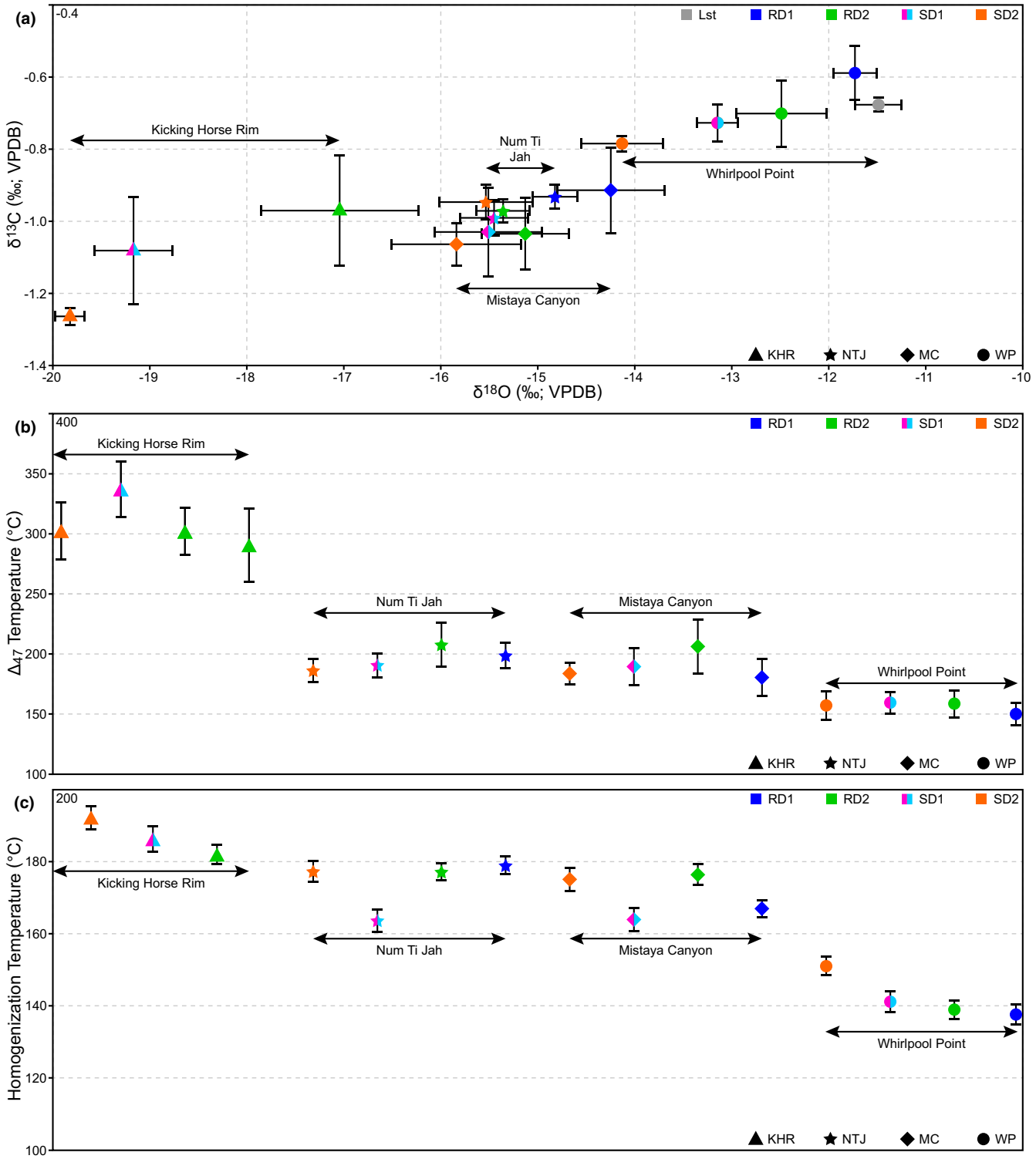

FIGURE 9 (a) $\delta^{13}C_{VPDB}$ vs. $\delta^{18}O_{VPDB}$ plot showing the progressive isotopic depletion from the platform interior to the platform margin. Note that Cambrian marine calcite (−10 to −4‰) and dolomite (−7 to −1‰) values plot outside of the region shown (Ryb & Eiler, 2018; Veizer & Prokoph, 2015). VDPB, Vienna Pee Dee Belemnite. (b) Clumped isotope crystallization temperature ($T\Delta_{47}$; Anderson et al., 2021) and (c) fluid inclusion homogenization temperature (T_h) plots showing the increase in temperature from the platform interior to the platform margin. Note that the $T\Delta_{47}$ values may have been affected by solid-state reordering (diffusion-driven isotopic exchange in the mineral lattice). Lst, limestone; RD, replacement dolomite; SD, saddle dolomite.

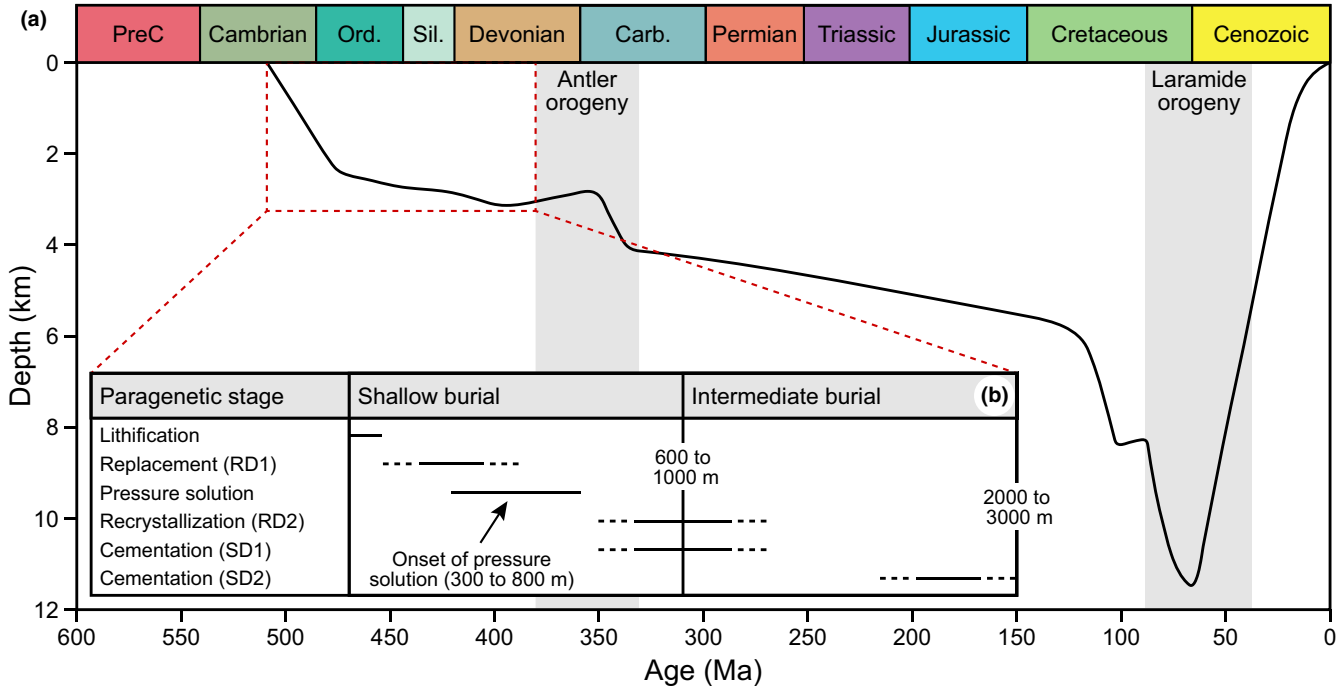

FIGURE 10 (a) Burial history diagram illustrating the Middle Cambrian strata in the Sukunka Front Ranges of the WCSB (modified from Vandeginste et al., 2007). (b) Interpreted paragenetic sequence based on the textural relationships in the Cathedral Formation and the Eldon Formation in the southern Rocky Mountains (WCSB). Note that the depths of the shallow burial and intermediate burial environments are from Machel (1999), whereas the onset of pressure solution is from Martín-Martín et al. (2018).

cementation. Applied to the WCSB, these features include the (i) absence of detrital quartz in SD (Table 2), (ii) sharp, symmetrical boundary between RD and SD (Figure 5a,b), (iii) isopachous growth of SD that are elongate and oriented perpendicular to the zebra texture (Figure 6), (iv) compositionally zoned crystals with euhedral terminations (Figure 7) and (v) presence of open porosity between the adjacent SD bands (Figure 5c,d). Such observations indicate that the formation of zebra textures involve the generation of cavities in the strata, as opposed to recrystallization without the formation of a cavity (cf. Centrella et al., 2022; Kelka et al., 2017).

At Whirlpool Point, opposing RD bands of the zebra textures are negative images of one another and would fit together if the SD bands were to be removed (Figure 5a,b); consistent with a fracture origin. This interpretation is analogous to other works on zebra textures (Gasparrini et al., 2006; Kareem et al., 2019; López-Horgue et al., 2009; Vandeginste et al., 2005; Wallace et al., 1994) and is consistent with their spatial relationship with faults (Figure 2b) and en échelon fractures (Figure 5a). However, there are several examples of zebra textures where the adjacent fracture walls do not match, particularly at the Kicking Horse Rim (Figure 5g,h). This observation suggests that the contact between RD and SD was dissolution enhanced (Morrow, 2014; Wallace & Hood, 2018) or underwent recrystallization (Centrella et al., 2022; Kelka et al., 2017). Evidence in support of recrystallization includes (i) the increased crystal size from RD1 to RD2 and (ii) the shift from oscillatory-zoned, planar-e dolomite to an unzoned mosaic of planar-s dolomite (Koeshidayatullah et al., 2020; Stacey et al., 2021). There is a spatial relationship between presence of RD2 and SD within the HTD bodies, which strongly suggests that the fluid flow event(s) that formed SD1 also gave rise to recrystallization of pre-existing dolomite in the strata (McCormick et al., 2021).

There is a marked shift in the character of the zebra textures, boxwork textures and dolomite breccias between Whirlpool Point (platform interior) and the Kicking Horse Rim (platform margin), which reflects the position of each locality relative to the source of the dolomitizing fluid (Figure 1d). Deformation in the platform interior gave rise to discrete faults, with minimal displacement, whereas the faults at the platform margin are more distributed and reflect their proximity to the epicentre of rifting (Cowie & Roberts, 2001; Gupta et al., 1998). At Whirlpool Point (Figure 5a,b), the zebra textures have textural characteristics that are similar to opening-mode, tensile fractures (cf. Brace, 1964; Ramsey & Chester, 2004). These opening-mode fractures are bedding-parallel, with SD crystals that are elongate and oriented perpendicular to the fracture surface (Figure 11). Porosity is preserved between adjacent SD bands, which indicates that the fractures

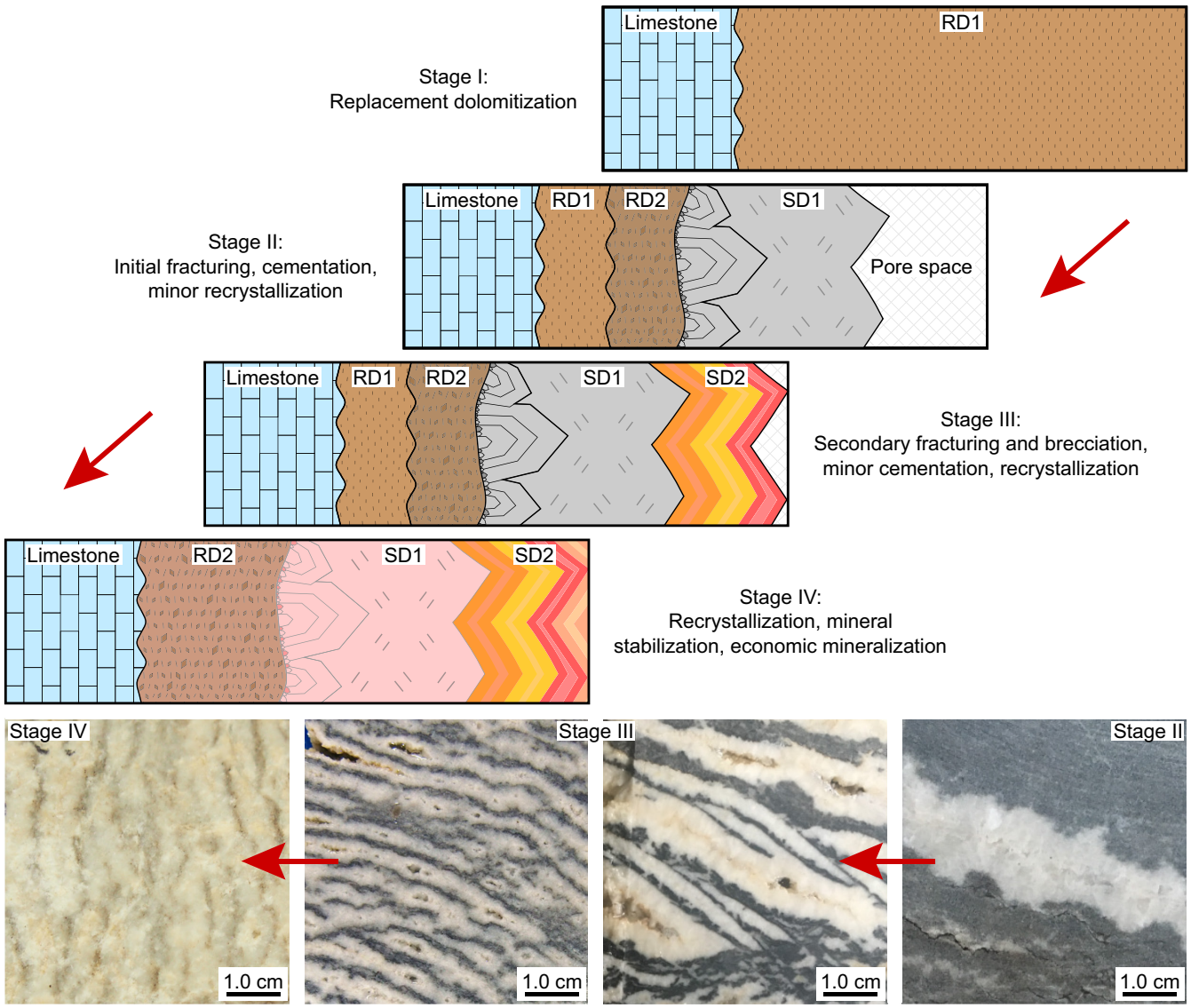

FIGURE 11 Conceptual model illustrating the multi-stage development of rock textures in HTD bodies. Stage I involves the replacement dolomitization of the host rock. Stage II involves dilatational fracturing, cementation and the formation of zebra textures (associated with minor recrystallization). Stage III involves secondary fracturing and the formation of boxwork textures and dolomite breccias (associated with significant recrystallization). Stage IV involves the final interval(s) of recrystallization, restricted to localities proximal to the fluid source, that may coincide with or pre-date economic mineralization.

formed by dilatation and cementation, rather than by displacive crystallization (cf. Merino et al., 2006; Merino & Canals, 2011). There is evidence of dilatation in the dolomite breccias, in which the clasts lack sorting, rotation or evidence for evaporite dissolution and likely did not form by collapse (Figure 2c,h,i).

At Mistaya Canyon and Num Ti Jah, the zebra textures are characterized by an increased fracture angle, but they have a strikingly constant inclination (Figure 5c,d). This increase in the fracture angle may reflect the transition from tensile failure to a mode of dilatant shear failure that occurs under low differential stresses, with high pore-fluid pressures (McCormick & Rutter, 2022; Ramsey & Chester, 2004). The fluid may have been focused into flow units that had a high lateral permeability relative to their vertical permeability, resulting in the localization of the zebra textures in individual beds (Figure 3a,b). Relative to zebra textures, boxwork textures are more porous, with highly irregular margins and evidence of clast rotation (Jacquemyn et al., 2014; Morrow, 2014). Boxwork textures are located only proximal to the fracture corridor at Mistaya Canyon and the contact between the Eldon Formation and the Pika Formation at Num Ti Jah (Figure 3d,h). This suggests that the Pika Formation acted as a low permeability seal and reactivity barrier as the fluid entered the Eldon Formation, leading to an increase in the pore-fluid pressure proximal to this contact. The irregular orientations of the RD in boxwork textures

are interpreted to reflect several fluid pulses entering the strata, which contribute to secondary fracturing and recrystallization (Figure 11).

At the Kicking Horse Rim, the HTD bodies are typically non-stratabound and comprise a strikingly high volume of SD, locally exceeding 80% of the strata (Figure 5i). Nevertheless, the bedding-surfaces are largely undisturbed with little evidence of dilatation. These volumetric constraints suggest that dilatational fracturing and cementation was not the predominant mechanism that formed the zebra textures and boxwork textures at the Kicking Horse Rim. RD2 is unzoned, forming an interlocking mosaic of nonplanar crystals. Petrographically, RD2 is also largely indistinguishable from SD1 (apart from their crystal sizes). Hence, these zebra textures may have been initiated as fractures, but recrystallization is interpreted to have largely overprinted their petrographical characteristics at the Kicking Horse Rim (Figure 11). As was the case for Num Ti Jah, the presence of a low permeability caprock likely influenced the pore-fluid pressure in the upper parts of the Cathedral Formation and, thus, dolomitization at the Kicking Horse Rim. Faults do not propagate through the mudstone and shale in the upper parts of the Cathedral Formation, nor do they intersect the Stephen Formation to circulate the dolomitizing fluid upwards into the Eldon Formation, which entirely comprises limestone.

6.3 | Basin scale fluid flow and its influence on the rock textures

At the basin scale, there is a spatial control on the development of the rock textures that is also reflected in the geochemical data. There is a clear trend of increasing temperature, recorded by both the clumped isotope and fluid inclusion analyses, from the platform interior to the platform margin (Figure 9b,c), which is consistent with the epicentre of rifting and associated crustal thinning in the vicinity of the Kicking Horse Rim (Aitken, 1971; Bond & Kominz, 1984; Powell et al., 2006). At Whirlpool Point, the $T\Delta_{47}$ values are higher than the T_h values by 5 to 20°C, which is due to pressure differences during the entrapment of fluid inclusions (Came et al., 2017; Honlet et al., 2018). Conversely, the $T\Delta_{47}$ values are higher than the T_h values by ca. 150°C at the Kicking Horse Rim, which may reflect the equilibration of $T\Delta_{47}$ through solid-state reordering (Hemingway & Henkes, 2021; Lloyd et al., 2018; Ryb et al., 2017). Such increasing temperature from the platform interior to the platform margin is also reflected in the dolomite geochemistry, which has led previous works to suggest that the dolomitizing fluid was sourced in the vicinity of the Kicking Horse Rim (Powell et al., 2006; Stacey et al., 2021; Vandeginste et al., 2007). $\delta^{18}O_{fluid}$ values, for example, increase from Whirlpool Point (2.8 to 4.6‰), to Mistaya Canyon and Num Ti Jah (2.9 to 5.4‰), to the Kicking Horse Rim (4.5 to 7.0‰). These $\delta^{18}O_{fluid}$ values plot between Middle Cambrian seawater (0 to −6‰; Veizer & Prokoph, 2015) and crustal fluids (2.2 to 11.5‰; Schulze et al., 2003), which led to the interpretation that dolomitization was mediated by seawater that mixed with a crustal-sourced brine (Koeshidayatullah et al., 2020; Stacey et al., 2021).

At Whirlpool Point, limestone has negative Ce/Ce* values that are consistent with early Palaeozoic seawater (Tostevin et al., 2016; Wallace et al., 2017). Ce/Ce* values in replacement dolomite can be inherited from the limestone (Hood et al., 2018), but extraneous dolomitizing fluids and high fluid-rock ratios can cause their REE signatures to deviate from the replaced lithology (Lottermoser, 1992; Qing & Mountjoy, 1994). There is a clear differentiation between the REE signatures of RD1 (Ce/Ce* = 0.852; Pr/Pr* = 1.07), RD2 (Ce/Ce* = 0.885; Pr/Pr* = 1.03) and SD1 (Ce/Ce* = 0.995; Pr/Pr* = 1.01), which indicates that each paragenetic stage formed by different processes. For replacement dolomite, the REE values can be partially inherited from the limestone, whereas the REE values entirely reflect the metasomatic fluid for a dolomite cement. RD2 plots between RD1 and SD1 because the REE signature of RD1 was progressively overprinted by the metasomatic fluid during recrystallization. Ce/Ce* anomalies are often used as a proxy for the redox state of fluids (Tostevin, 2021; Tostevin et al., 2016) and their increase from Whirlpool Point (0.796 to 0.995) to Mistaya Canyon and Num Ti Jah (0.883 to 0.994), to the Kicking Horse Rim (0.879 to 1.07), indicates that the dolomitizing fluid was more oxygenated in the platform interior relative to at the platform margin. This is consistent with a decreasing contribution of seawater to the dolomitizing fluid proximal to the Kicking Horse Rim (Figure 8e).

At Whirlpool Point, [Fe] and [Mn] are highly differentiated between each paragenetic stage and SD2 is notably enriched ([Fe] = 12,130 ppm, [Mn] = 1190 ppm) relative to the earlier, non-ferroan RD1, RD2 and SD1 (Figure 7a; Table 2). At the Kicking Horse Rim, [Fe] is significantly higher, reaching values up to 14,300 ppm and [Mn] is up to 2180 ppm (Figure 7a,d; Table 2). SD2 is also characterized by high Eu/Eu* (1.55 to 1.64; Figure 8f), which is largely analogous to the Eu/Eu* values of high temperature crustal fluids (Douville et al., 2002). Eu/Eu* in crustal fluids are influenced by temperature, pH, redox conditions and fluid–rock interaction (Douville et al., 1999, 2002). Therefore, the marked change in composition in SD2 suggests that (i) there was a change in the source of the dolomitizing fluid, or (ii) the dolomitizing fluid was subject to increased latency and fluid–rock interaction.

These geochemical relationships suggest that the dolomitizing fluid was seawater-dominated during the early stages of replacement dolomitization, potentially due to faults breaching the seafloor in the platform interior (cf. Hollis et al., 2017; Stacey et al., 2021). At the Kicking Horse Rim, the faults did not propagate through the upper parts of the Cathedral Formation and Stephen Formation, where the geochemical data indicate that dolomitization was caused by crustal fluids, probably sourced from deep-rooted basement faults. This shift in the fluid source is also reflected in the temperature of dolomitization, with the highest $T\Delta_{47}$ and T_h values in the vicinity of the Kicking Horse Rim (Figure 9b,c), where the associated crustal thinning gave rise to an elevated geothermal gradient (Johnston et al., 2009; Powell et al., 2006). The crustal fluids convected within the underlying Gog Group (Figure 1c,d; Stacey et al., 2021), mixed with seawater towards the platform interior and were emplaced upwards along faults into the Cathedral Formation, where they were distributed by thermal convection (cf. Benjakul et al., 2020; Hollis et al., 2017). The dolomitizing fluid became less seawater-dominated over time, with each paragenetic stage. This basin scale hydrogeological system is reflected in the rock textures, with replacement, fracturing and cementation interpreted as the governing processes within the platform interior (distal to the core of the rift and the source of the crustal fluids), whereas the contribution from recrystallization increasing towards the platform margin (proximal to the core of the rift and the source of the crustal fluids).

7 | DISCUSSION

There are a range of conceptual models that have been proposed to explain the formation of zebra textures, boxwork textures and dolomite breccias, including those that suggest that they form by the dissolution–replacement of sedimentological features (Beales & Hardy, 1980; Fontboté & Gorzawski, 1990; Krebs & Macqueen, 1984; Morrow, 2014), fracturing and cementation (López-Horgue et al., 2009; Nielsen et al., 1998; Swennen et al., 2012; Vandeginste et al., 2005; Wallace & Hood, 2018) and recrystallization (Centrella et al., 2022; Kelka et al., 2015, 2017). To systematically assess these interpretations, a multiple hypotheses approach (cf. Arnaud et al., 2022; Burgess et al., 2013) was used to evaluate the evidence for/against each of the proposed mechanisms (Figure 12a). Observations are tabulated in a matrix, and a decision ranking table was constructed to evaluate whether the evidence strongly supports (+1), weakly supports (+0.5), is neutral (0), weakly contradicts (−0.5), or strongly contradicts (−1) each interpretation. Hypotheses were broadly grouped into sedimentological (S), tectonic (T) and metasomatic (M) processes, and a series of ternary diagrams were constructed to evaluate how these processes vary between each locality (Figure 12b).

Numerous studies have recognized the effect of sedimentological parameters on HTD bodies (Humphrey et al., 2022; Koeshidayatullah et al., 2021; Sharp et al., 2010). HTD bodies often have stratabound terminations that correspond to sharp lithological contrasts between adjacent beds, which may occur due to the preferential flow of the dolomitizing fluid into higher permeability units. Lithological heterogeneities also affect the mechanical properties of the host rock because relatively incompetent, ductile lithologies limit the propagation of faults, resulting in the containment of fractures to more competent, brittle beds (Bowness et al., 2022). Such processes likely contributed to the largely stratabound orientation of the rock textures at Whirlpool Point, which transition to non-stratabound orientations at the Kicking Horse Rim (Figure 12a, row 1). It has also been noted that zebra textures are constrained to low porosity precursor limestones that had a higher horizontal permeability relative to their vertical permeability prior to dolomitization (Davies & Smith, 2006). Thus, there is commonly a relationship between the precursor sedimentary facies and the resulting rock textures (Figure 12a, row 2). For example, it was noted that bedding-parallel zebra textures are preferentially hosted in the highly anisotropic microbial boundstone facies at Whirlpool Point (Figure 2d,f), whereas bedding-inclined zebra textures are common in the bioturbated mudstone facies at Mistaya Canyon (Figures 3e and 5c). There is no apparent relationship between the precursor sedimentary facies and the zebra textures at the Kicking Horse Rim (Figure 4a). The presence of detrital quartz in RD1 and RD2, alongside the preservation of depositional textures, is evidence in favour of a sedimentological control on dolomitization (Figure 12, row 3). Overall, these sedimentological controls (Figure 12a,b) are interpreted to be significant at Whirlpool Point (+10), whereas they are negligible at the Kicking Horse Rim (−8).

The influence of tectonic features on dolomitization can vary depending on whether the fluid flow event(s) were pre-, syn- or post-kinematic because faults and fractures can act as conduits or barriers to fluid flow at different times (Iriarte et al., 2012; Kareem et al., 2019; Koeshidayatullah et al., 2022). In the WCSB, the geometries of the HTD bodies vary according to their proximity to the faults that intersect the strata (Stacey et al., 2021), and the spatial distributions of each paragenetic stage reflect these tectonic features (McCormick et al., 2021). Thus, Figure 12a (rows 4–6) qualitatively assesses these

(a)	Kicking Horse Rim (platform margin)			Whirlpool Point (platform interior)		
Observation	Sedimentological	Tectonic	Metasomatic	Sedimentological	Tectonic	Metasomatic
(1) Orientation of zebra textures are non-stratabound at the KHR, stratabound at WP	-0.5	+0.5	+0.5	+1	0	-1
(2) Zebra textures are facies independent at the KHR, facies dependent at WP	-0.5	+0.5	+0.5	+1	-0.5	-1
(3) RD1 and RD2 include detrital quartz, whereas quartz is absent in SD1 and SD2	+0.5	0	-0.5	+1	-0.5	-1
(4) Presence of zebra textures and dolomite breccias vary relative to fault proximity	-1	0	+0.5	+0.5	+1	-0.5
(5) En échelon fractures are common in the matrix proximal to zebra textures	-1	+0.5	0	-0.5	+1	-0.5
(6) Clasts in dolomite breccias and boxwork textures are fully surrounded by SD	-1	+0.5	-0.5	-0.5	+0.5	-0.5
(7) Zebra textures include multiple, texturally distinct, phases of dolomite	-1	0	+1	+1	+1	-0.5
(8) Increase in crystal size from the oscillatory zoned RD1 to the unzoned RD2	-0.5	0	+1	-0.5	0	+0.5
(9) Presence of RD2 is spatially related to the occurrence of SD1 throughout the strata	-1	+1	+1	-0.5	+0.5	+0.5
(10) SD crystals are elongate, with euhedral terminations into open pore space	-0.5	+0.5	+0.5	0	+1	-1
(11) Differentiated geochemical signatures between each paragenetic stage	-1	0	+1	+1	+1	-1
(12) RD/SD contact in zebra textures is distinct at WP, but it is obscure at the KHR	-1	-1	+1	+1	+1	-1
(13) RD clasts in breccias and boxwork textures have irregular margins	-1	-0.5	+1	-0.5	0	+0.5
(14) Stylolites are common in the matrix proximal to zebra textures	-0.5	0	+1	0	0	+0.5
Total	-10	+2	+8	+4	+6	-6

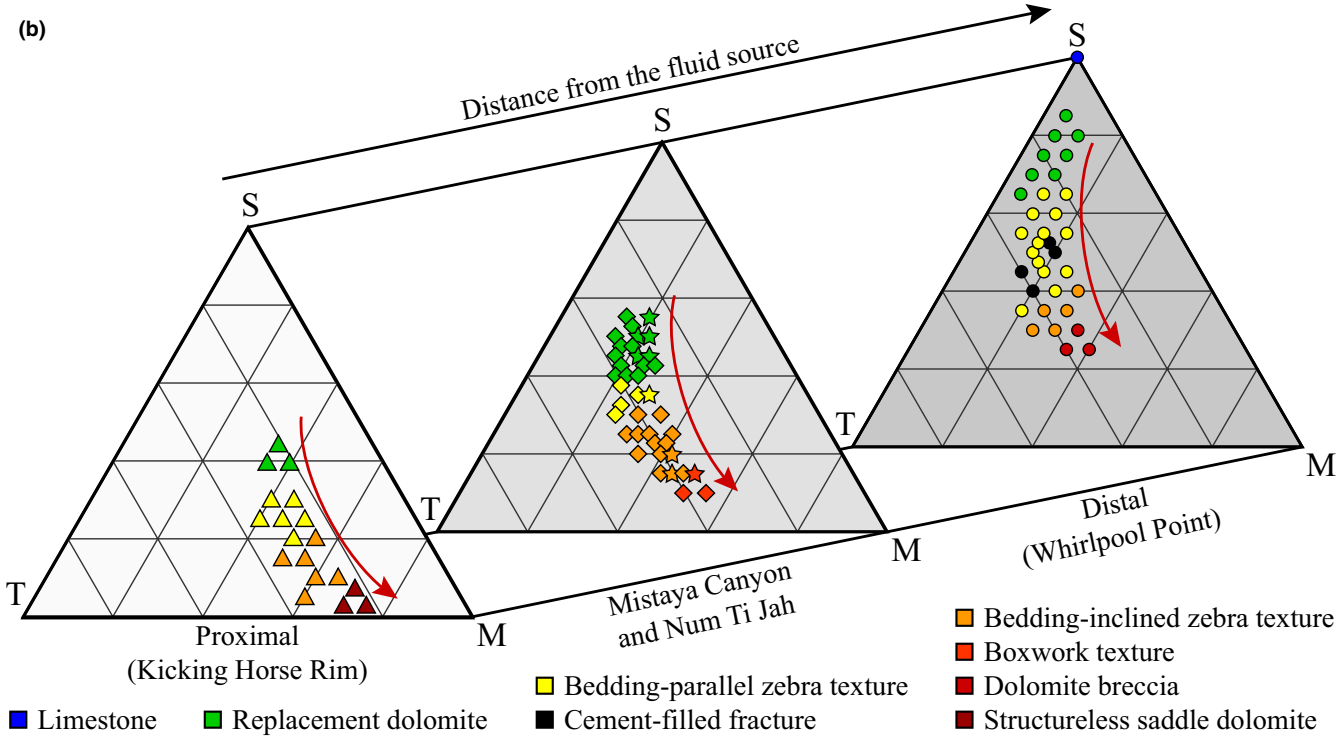

FIGURE 12 (a) Decision ranking table, following the method of Burgess et al. (2013) and Arnaud et al. (2022), used to assess the evidence for (+1) or against (−1) each process that may be involved in the formation of zebra textures, boxwork textures and dolomite breccias. (b) Ternary diagrams, illustrating the relative sedimentological, tectonic and metasomatic controls on the formation of these rock textures at each locality. Each of the samples from Whirlpool Point ($n = 35$), Mistaya Canyon ($n = 30$), Num Ti Jah ($n = 9$) and the Kicking Horse Rim ($n = 18$) were qualitatively assessed based on the criteria in Figure 12a. Each process is spatially and temporally variable, with the contribution from metasomatic processes increasing proximal to the source of the dolomitizing fluid.

relationships at each locality. At Whirlpool Point, the strata comprise bedding-parallel zebra textures, but the angle of these fractures (relative to bedding) systematically increases towards the platform margin, which reflects an increase in the effective differential stress (McCormick & Rutter, 2022; Ramsey & Chester, 2004). Koeshidayatullah et al. (2020) showed that as dolomitization progresses, matrix and fracture porosity is progressively occluded due to recrystallization and cementation, thus decreasing the permeability of the host rock and restricting the youngest paragenetic stages to the core of the HTD body. This interpretation is supported by the observation that boxwork textures and dolomite breccias are located only proximal to faults; Stacey et al. (2021) suggested that dolomite breccias form by the expulsion of overpressured fluids, upwards along faults, into a host rock that is confined by a low permeability caprock. The importance of vertical and lateral seals is evidenced by the increasing abundance of non-stratabound rock textures towards the contact with the Pika Formation at Num Ti Jah (Figure 3d), as well as the upper parts of the Cathedral Formation at the Kicking Horse Rim. The observation that the strata include multiple, texturally distinct phases of dolomite (Figure 12a, row 7) with highly differentiated geochemical signatures (Figure 12a, row 11) is also evidence in favour of a tectonic control on dolomitization. Overall, these tectonic controls (Figure 12a,b) are interpreted to be significant at Whirlpool Point (+6), whereas they are relatively minor at the Kicking Horse Rim (+2).

Metasomatism refers to compositional and mineralogical transformations, associated with chemical reactions triggered by a fluid, that affect a pre-existing rock (sensu Lesher & Spera, 2015). Replacement dolomitization is by definition metasomatic, but this section will focus on the evidence for recrystallization, which increases from Whirlpool Point (Figure 5a,b) to the Kicking Horse Rim (Figure 5f–i). As dolomitization progresses, ensuing fluid pulses contribute to the recrystallization of the pre-existing dolomite in the strata (Koeshidayatullah et al., 2020; McCormick et al., 2021; Stacey et al., 2021). In zebra textures (Figure 12a, row 8), recrystallization is denoted by the shift from RD1 (concentrically zoned, planar-e to planar-s dolomite) to an interlocking mosaic of RD2 (weakly zoned to unzoned, planar-s to nonplanar dolomite). The change in texture between RD1 and RD2 is accompanied by an increase in crystal size because dissolution-precipitation is driven by a reduction of surface free energy (Gregg et al., 1992; Machel, 1997; Ryan et al., 2022). The occurrence of RD2 in the strata is spatially associated with SD1, which indicates that they formed from the same fluid flow event (Figure 12a, row 9). The observation that RD2 has a similar trace element and stable isotopic composition as SD1, typical of zebra textures elsewhere (Wallace & Hood, 2018), is also consistent with recrystallization. Recrystallization from RD1 to RD2 is associated with an increase in crystal size. At the Kicking Horse Rim, however, there is a narrow region of decreased crystal size along the boundary between RD2 and SD1 (Figure 6h). Such crystal size reduction is characteristic of dynamic recrystallization, a process driven by both strain energy and surface free energy (Newman & Mitra, 1994). The high temperatures encountered at the Kicking Horse Rim (>200°C), similar to those modelled by Centrella et al. (2022), may have led to dynamic recrystallization alongside the solid-state reordering of Δ_{47}; processes likely to occur in HTD bodies that are subject to P/T conditions approaching low-grade metamorphism. Overall, these metasomatic controls (Figure 12a, rows 12–14) are interpreted to be minor at Whirlpool Point (−6), whereas they are highly evident at the Kicking Horse Rim (+8).

Over the past 30 years, a large body of literature has proposed models to explain the formation of zebra textures (Wallace & Hood, 2018, and references therein); most of which are based on specific features from a small number of samples and localities. The basin scale approach presented in this study (tens to hundreds of kilometres in extent) demonstrates that the properties of zebra textures, boxwork textures and dolomite breccias can vary significantly between localities. Although each of these models may be applicable to the zebra textures at a given locality, they do not uniquely explain all the rock textures that are encountered across the basin (Figure 12a,b). At Whirlpool Point (distal to the fluid source), these rock textures formed due to dilatational fracturing and the precipitation of SD as a cement (Figure 5a,b). Their spatial relationship with faults supports the interpretation that there is an over-riding tectonic control on the occurrence of zebra textures, boxwork textures and dolomite breccias in HTD bodies. Nevertheless, there is evidence that the precursor sedimentological texture at Whirlpool Point influenced the flow of dolomitizing fluid away from faults and the mechanical properties of the strata, thus influencing the distribution and characteristics of zebra textures. At Mistaya Canyon and Num Ti Jah, the increasing fracture angles forming the zebra textures reflect the higher pore-fluid pressures proximal to lithological seals and/or the increased proximity to the source of the dolomitizing fluid (Figure 5c–e). There is a marked shift in the petrography and geochemistry of the rock textures at the Kicking Horse Rim (Figure 5f–i), interpreted to be due to pervasive metasomatism. Similar rock textures to those in the platform interior may have preceded this recrystallization, but it is challenging to establish the precursor lithology. Nevertheless, the exceptionally high

dolomitization temperatures, volume of SD and confinement of dolomitization to the Cathedral Formation, indicates that the strata at the Kicking Horse Rim have undergone significant recrystallization. In conclusion, there is no conceptual model that is a 'silver bullet' that explains all the characteristics of these rock textures (Figure 12a,b). Classical zebra textures are located within the platform interior facies, furthest from the core of the rift and the source of the dolomitizing fluid, whereas significant recrystallization can occur during the later stages of dolomitization, due to the flux of several pulses of hot, crustal fluid into the strata. Such recrystallization may occur immediately after the first phase of dolomitization, or at an indefinite point in the burial history of a basin.

8 | CONCLUSIONS

Rock textures in fault-controlled, HTD bodies are petrographical and geochemical archives of multi-phase dolomitization, recrystallization and cementation. Such reactions fingerprint the spatial and temporal evolution of fluids in a sedimentary basin and provide critical insights into sedimentological, tectonic and metasomatic processes. This study investigated the evolution of zebra textures, boxwork textures and dolomite breccias in the Middle Cambrian strata in the WCSB. The basin scale petrographical and geochemical analysis of these rock textures has led to the following important conclusions:

1. Each of the published models for the formation of zebra textures (and those of associated rock textures) fail to explain at least one of their characteristics. However, the general features of these models can be grouped into ternary diagrams that can differentiate a wider array of rock textures, placing them in context of the proximity to the fluid source.
2. Sedimentological heterogeneities affect the permeability of the host rock, which preferentially focuses the dolomitizing fluid(s) into individual stratabound units and locally influences the pore-fluid pressure during dolomitization and cementation.
3. There is clear evidence that brittle failure is involved in the formation of these rock textures. Models solely based on fracturing, however, fail to account for the volume expansion and mass-balance constraints required to accommodate such a process.
4. With each successive fluid pulse, faults and fractures in the strata can be reactivated and subject to recrystallization, therefore forming increasingly complex rock textures.
5. At the outcrop scale, the relative importance of each process changes with each successive fluid pulse and, thus, each paragenetic stage. This trend is also present at the basin scale, with sedimentological and tectonic controls at the platform interior that are increasingly affected by metasomatic processes towards the platform margin.

In summary, the petrographical and geochemical evidence presented in this study indicates that zebra textures, boxwork textures and dolomite breccias are initiated due to dilatational fracturing and the precipitation of SD as a cement, but significant recrystallization can occur during the later stages of dolomitization, largely overprinting these rock textures. The physio-chemical properties of zebra textures vary with respect to their proximity to the source of the dolomitizing fluid, thus providing critical information to predict the distribution of carbonate-hosted ore deposits and reservoir properties for energy exploitation and carbon storage.

ACKNOWLEDGEMENTS

This work was conducted as part of C. A. McCormick's doctoral research, funded by the President's Doctoral Scholar Award (The University of Manchester). We are grateful to Parks Canada and Alberta Tourism, Parks and Recreation for the research and collection permits. $\delta^{13}C$, $\delta^{18}O$ and Δ_{47} analyses were made possible by a National Environmental Isotope Facility grant from the Natural Environment Research Council (NERC). The authors acknowledge The University of Manchester and the Science and Technology Facilities Council (#ST/S002170/1) for funding the LA ICP-MS facility and the NERC-funded Nanoscale Imaging and Analysis Facility for Environmental Materials in the Williamson Research Centre for Molecular Environmental Science (NERC CC042). We are indebted to John Waters and Jonathan Fellows (The University of Manchester) who conducted the X-ray diffraction and electron-probe micro-analysis, respectively. Additional support to C.A. McCormick came from the Society for Sedimentary Geology Foundation (Student Research Grant), the International Association of Sedimentologists (Postgraduate Research Grant), the British Sedimentological Research Group (Trevor Elliot Memorial Grant) and the American Association of Petroleum Geologists Foundation (Classen Family Named Grant). We are grateful for the careful reviews on an earlier version of this manuscript that were provided by Dr. Malcolm Wallace and two anonymous reviewers, as well as for the comments from the Editor, Dr. Atle Rotevatn.

CONFLICT OF INTEREST STATEMENT

The authors declare that they have no known competing financial interests or personal relationships that could have appeared to influence the work reported in this paper.

PEER REVIEW

The peer review history for this article is available at https://www.webofscience.com/api/gateway/wos/peer-review/10.1111/bre.12789.

DATA AVAILABILITY STATEMENT

All data used for this research are described in the article or available as supplementary material.

ORCID

Cole A. McCormick https://orcid.org/0000-0003-2176-3122
Hilary Corlett https://orcid.org/0000-0002-3518-4618
Matthieu Clog https://orcid.org/0000-0003-3001-8909
Adrian J. Boyce https://orcid.org/0000-0002-9680-0787
Romain Tartèse https://orcid.org/0000-0002-3490-9875
Matthew Steele-MacInnis https://orcid.org/0000-0001-5053-9344
Cathy Hollis https://orcid.org/0000-0002-3980-2583

REFERENCES

Aitken, J. D. (1971). Control of lower Paleozoic sedimentary facies by the Kicking Horse Rim, southern Rocky Mountains, Canada. *Bulletin of Canadian Petroleum Geology*, *19*, 557–569.

Aitken, J. D. (1989). Birth, growth and death of the Middle Cambrian Cathedral carbonate lithosome, Southern Rocky Mountains. *Bulletin of Canadian Petroleum Geology*, *37*(3), 316–333.

Aitken, J. D. (1997). Stratigraphy of the Middle Cambrian platformal succession, southern Rocky Mountains. *Geological Survey of Canada Bulletin*, *398*, 1–322.

Anderson, N. T., Kelson, J. R., Kele, S., Daëron, M., Bonifacie, M., Horita, J., Mackey, T. J., John, C. M., Kluge, T., Petschnig, P., Jost, A. B., Huntington, K. W., Bernasconi, S. M., & Bergmann, K. D. (2021). A unified clumped isotope thermometer calibration (0.5–1,100 C) using carbonate-based standardization. *Geophysical Research Letters*, *48*(7), e2020GL092069.

Arnaud, G., Burgess, P., Bosence, D., & Hollis, C. (2022). Broken beds but better science: Using multiple hypotheses to interpret geological data. *Terra Nova*, *00*, 1–10.

Beales, F. W., & Hardy, J. L. (1980). Criteria for the recognition of diverse dolomite types with an emphasis on studies of host rocks for Mississippi Valley-type ore deposits. In D. H. Zenger, J. B. Dunham, & R. L. Ethington (Eds.), *Concepts and models of dolomitization* (SEPM Special Publication, Vol. *28*, pp. 197–213). Society of Economic Paleontologists and Mineralogists.

Benjakul, R., Hollis, C., Robertson, H. A., Sonnenthal, E. L., & Whitaker, F. F. (2020). Understanding controls on hydrothermal dolomitisation: Insights from 3D reactive transport modelling of geothermal convection. *Solid Earth*, *11*(6), 2439–2461.

Bernasconi, S. M., Daëron, M., Bergmann, K. D., Bonifacie, M., Meckler, A. N., Affek, H. P., Anderson, N., Bajnai, D., Barkan, E., Beverly, E., Blamart, D., Burgener, L., Calmels, D., Chaduteau, C., Clog, M., Davidheiser-Kroll, B., Davies, A., Dux, F., Eiler, J., … Ziegler, M. (2021). InterCarb: A community effort to improve inter-laboratory standardization of the carbonate clumped isotope thermometer using carbonate standards. *Geochemistry, Geophysics, Geosystems*, *22*(5), e2020GC009588.

Bond, G. C., Christie-Blick, N., Kominz, M. A., & Devlin, W. J. (1985). An early Cambrian rift to post-rift transition in the Cordillera of western North America. *Nature*, *315*(6022), 742–746.

Bond, G. C., & Kominz, M. A. (1984). Construction of tectonic subsidence curves for the early Paleozoic miogeocline, southern Canadian Rocky Mountains: Implications for subsidence mechanisms, age of breakup, and crustal thinning. *Geological Society of America Bulletin*, *95*(2), 155–173.

Boni, M., Iannace, A., Bechstädt, T., & Gasparrini, M. (2000). Hydrothermal dolomites in SW Sardinia (Italy) and Cantabria (NW Spain): Evidence for late-to post-Variscan widespread fluid-flow events. *Journal of Geochemical Exploration*, *69*, 225–228.

Bowness, N. P., Cawood, A. J., Ferrill, D. A., Smart, K. J., & Bellow, H. B. (2022). Mineralogy controls fracture containment in mechanically layered carbonates. *Geological Magazine*, *159*, 1–19.

Brace, W. F. (1964). Brittle fracture of rocks. In W. R. Judd (Ed.), *State of stress in Earth's crust* (pp. 111–180). Elsevier.

Brand, W. A., Assonov, S. S., & Coplen, T. B. (2010). Correction for the ^{17}O interference in $\delta^{13}C$ measurements when analyzing CO_2 with stable isotope mass spectrometry (IUPAC technical report). *Pure and Applied Chemistry*, *82*, 1719–1733.

Breislin, C. J., Banks, V. J., Crowley, S. F., Marshall, J. D., Millar, I., Riding, J. B., & Hollis, C. E. (2022). Mechanisms controlling the localization of fault-controlled hydrothermal dolomitization, Derbyshire platform, UK. *The Depositional Record*, *00*, 1–25.

Burgess, P. M., Winefield, P., Minzoni, M., & Elders, C. (2013). Methods for identification of isolated carbonate buildups from seismic reflection data. *American Association of Petroleum Geologists Bulletin*, *97*(7), 1071–1098.

Came, R. E., Azmy, K., Tripati, A., & Olanipekun, B. J. (2017). Comparison of clumped isotope signatures of dolomite cements to fluid inclusion thermometry in the temperature range of 73–176 C. *Geochimica et Cosmochimica Acta*, *199*, 31–47.

Centrella, S., Beaudoin, N. E., Derluyn, H., Motte, G., Hoareau, G., Lanari, P., Piccoli, F., Pecheyran, C., & Callot, J. P. (2021). Micro-scale chemical and physical patterns in an interface of hydrothermal dolomitization reveals the governing transport mechanisms in nature: Case of the Layens anticline, Pyrenees, France. *Sedimentology*, *68*(2), 834–854.

Centrella, S., Beaudoin, N. E., Koehn, D., Motte, G., Hoareau, G., & Callot, J. P. (2022). How fluid-mediated rock transformations can mimic hydro-fracturing patterns in hydrothermal dolomite. *Marine and Petroleum Geology*, *140*, 105657.

Collom, C. J., Johnston, P. A., & Powell, W. G. (2009). Reinterpretation of 'middle' Cambrian stratigraphy of the rifted western Laurentian margin: Burgess Shale Formation and contiguous units (Sauk II megasequence), Rocky Mountains, Canada. *Palaeogeography, Palaeoclimatology, Palaeoecology*, *277*, 63–85.

Cowie, P. A., & Roberts, G. P. (2001). Constraining slip rates and spacings for active normal faults. *Journal of Structural Geology*, *23*(12), 1901–1915.

Davies, A. J., & John, C. M. (2017). Reducing contamination parameters for clumped isotope analysis: The effect of

lowering Porapak™ Q trap temperature to below −50 C. *Rapid Communications in Mass Spectrometry*, *31*(16), 1313–1323.

Davies, G. R., & Smith, L. B., Jr. (2006). Structurally controlled hydrothermal dolomite reservoir facies: An overview. *American Association of Petroleum Geologists Bulletin*, *90*, 1641–1690.

Dewit, J., Foubert, A., El Desouky, H. A., Muchez, P., Hunt, D., Vanhaecke, F., & Swennen, R. (2014). Characteristics, genesis and parameters controlling the development of a large stratabound HTD body at Matienzo (Ramales platform, Basque–Cantabrian Basin, northern Spain). *Marine and Petroleum Geology*, *55*, 6–25.

Dickson, J. A. D. (1966). Carbonate identification and genesis as revealed by staining. *Journal of Sedimentary Research*, *36*, 491–505.

Douville, E., Bienvenu, P., Charlou, J. L., Donval, J. P., Fouquet, Y., Appriou, P., & Gamo, T. (1999). Yttrium and rare earth elements in fluids from various deep-sea hydrothermal systems. *Geochimica et Cosmochimica Acta*, *63*(5), 627–643.

Douville, E., Charlou, J. L., Oelkers, E. H., Bienvenu, P., Colon, C. J., Donval, J. P., Fouquet, Y., Prieur, D., & Appriou, P. (2002). The rainbow vent fluids (36 140 N, MAR): The influence of ultramafic rocks and phase separation on trace metal content in mid-Atlantic ridge hydrothermal fluids. *Chemical Geology*, *184*, 37–48.

Duggan, J. P., Mountjoy, E. W., & Stasiuk, L. D. (2001). Fault-controlled dolomitization at Swan Hills Simonette oil field (Devonian), deep basin west-Central Alberta, Canada. *Sedimentology*, *48*(2), 301–323.

Fontboté, L., & Gorzawski, H. (1990). Genesis of the Mississippi Valley-type Zn-Pb deposit of San Vicente, Central Peru; geologic and isotopic (Sr, O, C, S, Pb) evidence. *Economic Geology*, *85*, 1402–1437.

Gabellone, T., Iannace, A., & Gasparrini, M. (2014). Multiple dolomitization episodes in deep-water limestones of the Triassic Lagonegro basin (southern Italy): From early reflux to tectonically driven fluid flow. *Journal of Sedimentary Research*, *84*, 435–456.

Gasparrini, M., Bechstädt, T., & Boni, M. (2006). Massive hydrothermal dolomites in the southwestern Cantabrian zone (Spain) and their relation to the late Variscan evolution. *Marine and Petroleum Geology*, *23*, 543–568.

Goldstein, R. H., & Reynolds, T. J. (1994). *Systematics of fluid inclusions in diagenetic minerals*. Short course 31, 199 p. Society of Economic Paleontologists and Mineralogists.

Gregg, J. M., Howard, S. A., & Mazzullo, S. J. (1992). Early diagenetic recrystallization of Holocene (<3000 years old) peritidal dolomites, Ambergris Cay, Belize. *Sedimentology*, *39*(1), 143–160.

Gupta, S., Cowie, P. A., Dawers, N. H., & Underhill, J. R. (1998). A mechanism to explain rift-basin subsidence and stratigraphic patterns through fault-array evolution. *Geology*, *26*(7), 595–598.

Hemingway, J. D., & Henkes, G. A. (2021). A disordered kinetic model for clumped isotope bond reordering in carbonates. *Earth and Planetary Science Letters*, *566*, 116962.

Hendry, J. P., Gregg, J. M., Shelton, K. L., Somerville, I. D., & Crowley, S. F. (2015). Origin, characteristics and distribution of fault-related and fracture-related dolomitization: Insights from Mississippian carbonates, Isle of Man. *Sedimentology*, *62*(3), 717–752.

Hiemstra, E. J., & Goldstein, R. H. (2015). Repeated injection of hydrothermal fluids into downdip carbonates: A diagenetic and stratigraphic mechanism for localization of reservoir porosity, Indian Basin field, New Mexico, USA. *Geological Society, London, Special Publications*, *406*(1), 141–177.

Hirani, J., Bastesen, E., Boyce, A., Corlett, H., Gawthorpe, R., Hollis, C., John, C. M., Robertson, H., Rotevatn, A., & Whitaker, F. (2018). Controls on the formation of stratabound dolostone bodies, Hammam Faraun fault block, Gulf of Suez. *Sedimentology*, *65*(6), 1973–2002.

Hollis, C., Bastesen, E., Boyce, A., Corlett, H., Gawthorpe, R., Hirani, J., Rotevatn, A., & Whitaker, F. (2017). Fault-controlled dolomitization in a rift basin. *Geology*, *45*(3), 219–222.

Honlet, R., Gasparrini, M., Muchez, P., Swennen, R., & John, C. M. (2018). A new approach to geobarometry by combining fluid inclusion and clumped isotope thermometry in hydrothermal carbonates. *Terra Nova*, *30*(3), 199–206.

Hood, A. vS., Planavsky, N.J., Wallace, M.W., Wang, X., 2018. The effects of diagenesis on geochemical paleoredox proxies in sedimentary carbonates. *Geochimica et Cosmochimica Acta*, *232*, 265–287.

Horita, J. (2014). Oxygen and carbon isotope fractionation in the system dolomite–water–CO2 to elevated temperatures. *Geochimica et Cosmochimica Acta*, *129*, 111–124.

Howell, D., Griffin, W. L., Pearson, N. J., Powell, W., Wieland, P., & O'Reilly, S. Y. (2013). Trace element partitioning in mixed-habit diamonds. *Chemical Geology*, *355*, 134–143.

Humphrey, E., Gomez-Rivas, E., Martín-Martín, J. D., Neilson, J., Salas, R., & Guimerà, J. (2022). Depositional and structural controls on a fault-related dolostone formation (Maestrat Basin, E Spain). *Basin Research*, *34*(2), 961–990.

Iannace, A., Gasparrini, M., Gabellone, T., & Mazzoli, S. (2012). Late dolomitization in basinal limestones of the southern Apennines fold and thrust belt (Italy). *Oil & gas Science and Technology–Revue d'IFP Energies Nouvelles*, *67*(1), 59–75.

Iriarte, E., Lopez-Horgue, M. A., Schroeder, S., & Caline, B. (2012). Interplay between fracturing and hydrothermal fluid flow in the Asón Valley hydrothermal dolomites (Basque Cantabrian Basin, Spain). *Geological Society, London, Special Publications*, *370*(1), 207–227.

Jacquemyn, C., El Desouky, H., Hunt, D., Casini, G., & Swennen, R. (2014). Dolomitization of the Latemar platform: Fluid flow and dolomite evolution. *Marine and Petroleum Geology*, *55*, 43–67.

Jochum, K. P., Garbe-Schönberg, D., Veter, M., Stoll, B., Weis, U., Weber, M., Lugli, F., Jentzen, A., Schiebel, R., Wassenburg, J. A., Jacob, D. E., & Haug, G. H. (2019). Nano-powdered calcium carbonate reference materials: Significant progress for microanalysis? *Geostandards and Geoanalytical Research*, *43*(4), 595–609.

Jochum, K. P., Weis, U., Stoll, B., Kuzmin, D., Yang, Q., Raczek, I., Jacob, D. E., Stracke, A., Birbaum, K., Frick, D. A., Günther, D., & Enzweiler, J. (2011). Determination of reference values for NIST SRM 610–617 glasses following ISO guidelines. *Geostandards and Geoanalytical Research*, *35*(4), 397–429.

John, C. M., & Bowen, D. (2016). Community software for challenging isotope analysis: First applications of 'Easotope' to clumped isotopes. *Rapid Communications in Mass Spectrometry*, *30*(21), 2285–2300.

Johnston, P. A., Johnston, K. J., Collom, C. J., Powell, W. G., & Pollock, R. J. (2009). Palaeontology and depositional environments of ancient brine seeps in the Middle Cambrian Burgess Shale at The Monarch, British Columbia, Canada.

Palaeogeography, Palaeoclimatology, Palaeoecology, *277*, 86–105.

Kareem, K. H., Al-Aasm, I. S., & Mansurbeg, H. (2019). Structurally-controlled hydrothermal fluid flow in an extensional tectonic regime: A case study of cretaceous Qamchuqa formation, Zagros Basin, Kurdistan Iraq. *Sedimentary Geology*, *386*, 52–78.

Kelka, U., Koehn, D., & Beaudoin, N. (2015). Zebra pattern in rocks as a function of grain growth affected by second-phase particles. *Frontiers in Physics*, *3*, 1–14.

Kelka, U., Veveakis, M., Koehn, D., & Beaudoin, N. (2017). Zebra rocks: Compaction waves create ore deposits. *Scientific Reports*, *7*(1), 1–9.

Koeshidayatullah, A., Al-Sinawi, N., Swart, P. K., Boyce, A., Redfern, J., & Hollis, C. (2022). Coevolution of diagenetic fronts and fluid-fracture pathways. *Scientific Reports*, *12*(1), 1–11.

Koeshidayatullah, A., Corlett, H., & Hollis, C. (2021). An overview of structurally-controlled dolostone-limestone transitions in the stratigraphic record. *Earth-Science Reviews*, *220*, 103751.

Koeshidayatullah, A., Corlett, H., Stacey, J., Swart, P. K., Boyce, A., & Hollis, C. (2020). Origin and evolution of fault-controlled hydrothermal dolomitization fronts: A new insight. *Earth and Planetary Science Letters*, *541*, 116291.

Krebs, W., & Macqueen, R. (1984). Sequence of diagenetic and mineralization events, pine point lead-zinc property, Northwest Territories, Canada. *Bulletin of Canadian Petroleum Geology*, *32*, 434–464.

Lesher, C. E., & Spera, F. J. (2015). Thermodynamic and transport properties of silicate melts and magma. In H. Sigurdsson, B. Houghton, S. R. McNutt, H. Rymer, & J. Stix (Eds.), *The encyclopedia of volcanoes* (pp. 113–141). Academic Press.

Lloyd, M. K., Ryb, U., & Eiler, J. M. (2018). Experimental calibration of clumped isotope reordering in dolomite. *Geochimica et Cosmochimica Acta*, *242*, 1–20.

Lonnee, J., & Machel, H. G. (2006). Pervasive dolomitization with subsequent hydrothermal alteration in the Clarke Lake gas field, middle Devonian slave point formation, British Columbia, Canada. *American Association of Petroleum Geologists Bulletin*, *90*(11), 1739–1761.

López-Horgue, M. A., Iriarte, E., Schröder, S., Fernández-Mendiola, P. A., Caline, B., Corneyllie, H., Frémont, J., Sudrie, M., & Zerti, S. (2010). Structurally controlled hydrothermal dolomites in Albian carbonates of the Asón valley, Basque Cantabrian Basin. *Northern Spain. Marine and Petroleum Geology*, *27*(5), 1069–1092.

López-Horgue, M. A., Iriarte, E., Schroeder, S., Caline, B., & Fernández Mendiola, P. Á. (2009). An example on the tectonic origin of zebra dolomites: The San Martín beach outcrop (Santoña, North Spain). *Geogaceta*, *47*, 85–88.

Lottermoser, B. G. (1992). Rare earth elements and hydrothermal ore formation processes. *Ore Geology Reviews*, *7*(1), 25–41.

Machel, H. G. (1997). Recrystallization versus neomorphism, and the concept of 'significant recrystallization' in dolomite research. *Sedimentary Geology*, *113*(3–4), 161–168.

Machel, H. G. (1999). Effects of groundwater flow on mineral diagenesis, with emphasis on carbonate aquifers. *Hydrogeology Journal*, *7*, 94–107.

Machel, H. G. (2004). Concepts and models of dolomitization: A critical reappraisal. *Geological Society, London, Special Publications*, *235*(1), 7–63.

Machel, H. G., & Lonnee, J. (2002). Hydrothermal dolomite—A product of poor definition and imagination. *Sedimentary Geology*, *152*(3–4), 163–171.

Martín-Martín, J. D., Gomez-Rivas, E., Gómez-Gras, D., Travé, A., Ameneiro, R., Koehn, D., & Bons, P. D. (2018). Activation of stylolites as conduits for overpressured fluid flow in dolomitized platform carbonates. *Geological Society, London, Special Publications*, *459*(1), 157–176.

Martín-Martín, J. D., Travé, A., Gomez-Rivas, E., Salas, R., Sizun, J. P., Vergés, J., Corbella, M., Stafford, S. L., & Alfonso, P. (2015). Fault-controlled and stratabound dolostones in the late Aptian–earliest Albian Benassal formation (Maestrat Basin, E Spain): Petrology and geochemistry constrains. *Marine and Petroleum Geology*, *65*, 83–102.

McCormick, C. A., Corlett, H., Stacey, J., Hollis, C., Feng, J., Rivard, B., & Omma, J. E. (2021). Shortwave infrared hyperspectral imaging as a novel method to elucidate multi-phase dolomitization, recrystallization, and cementation in carbonate sedimentary rocks. *Scientific Reports*, *11*(1), 1–16.

McCormick, C. A., & Rutter, E. H. (2022). An experimental study of the transition from tensile failure to shear failure in Carrara marble and Solnhofen limestone: Does "hybrid failure" exist? *Tectonophysics*, *844*, 229623.

McMechan, M. E. (2022). Structural geometry and kinematic history of the southern Kicking Horse Rim Cambrian carbonate platform: Out-of-sequence thrust faulting in the southern Canadian Rocky Mountains. *Bulletin of Canadian Petroleum Geology*, *69*(1), 51–72.

Merino, E., & Canals, À. (2011). Self-accelerating dolomite-for-calcite replacement: Self-organized dynamics of burial dolomitization and associated mineralization. *American Journal Science*, *311*(7), 573–607.

Merino, E., Fletcher, R., & Canals, À. (2006). Genesis of self-organized zebra textures in burial dolomites: Displacive veins, induced stress, and dolomitization. *Geologica Acta*, *4*, 383–393.

Morrow, D. W. (2014). Zebra and boxwork fabrics in hydrothermal dolomites of northern Canada: Indicators for dilational fracturing, dissolution or in situ replacement? *Sedimentology*, *61*, 915–951.

Nance, W. B., & Taylor, S. R. (1976). Rare earth element patterns and crustal evolution–I. Australian post-Archean sedimentary rocks. *Geochimica et Cosmochimica Acta*, *40*(12), 1539–1551.

Newman, J., & Mitra, G. (1994). Fluid-influenced deformation and recrystallization of dolomite at low temperatures along a natural fault zone, Mountain City window, Tennessee. *Geological Society of America Bulletin*, *106*(10), 1267–1280.

Nielsen, P., Swennen, R., Muchez, P., & Keppens, E. (1998). Origin of Dinantian zebra dolomites south of the Brabant-Wales Massif, Belgium. *Sedimentology*, *45*, 727–743.

Paradis, S., & Simandl, G. J. (2017). Are there genetic links between carbonate-hosted barite-zinc-lead sulphide deposits and magnesite mineralization in Southeast British Columbia? In N. Rogers (Ed.), *Targeted geoscience initiative: 2017 report of activities* (Geological Survey of Canada, Open File, Vol. *8358*, pp. 217–227). Geological Survey of Canada.

Paton, C., Hellstrom, J., Paul, B., Woodhead, J., & Hergt, J. (2011). Iolite: Freeware for the visualisation and processing of mass spectrometric data. *Journal of Analytical Atomic Spectrometry*, *26*(12), 2508–2518.

Petersen, S. V., Defliese, W. F., Saenger, C., Daëron, M., Huntington, K. W., John, C. M., Kelson, J. R., Bernasconi, S. M., Colman, A. S., Kluge, T., Olack, G. A., Schauer, A. J., Bajnai, D., Bonifacie, M., Breitenbach, S. F. M., Fiebig, J., Fernandez, A. B., Henkes, G. A., Hodell, D., … Winkelstern, I. Z. (2019). Effects of improved ^{17}O correction on interlaboratory agreement in clumped isotope calibrations, estimates of mineral-specific offsets, and temperature dependence of acid digestion fractionation. *Geochemistry, Geophysics, Geosystems*, *20*(7), 3495–3519.

Powell, W. G., Johnston, P. A., Collom, C. J., & Johnston, K. J. (2006). Middle Cambrian brine seeps on the Kicking Horse Rim and their relationship to talc and magnesite mineralization and associated dolomitization, British Columbia, Canada. *Economic Geology*, *101*, 431–451.

Pratt, B. R. (2002). Teepees in peritidal carbonates: Origin via earthquake-induced deformation, with example from the Middle Cambrian of western Canada. *Sedimentary Geology*, *153*, 57–64.

Price, R. (1981). The cordilleran foreland thrust and fold belt in the southern Canadian Rocky Mountains. *Geological Society, London, Special Publications*, *9*(1), 427–448.

Putnis, A. (2002). Mineral replacement reactions: From macroscopic observations to microscopic mechanisms. *Mineralogical Magazine*, *66*(5), 689–708.

Qing, H., & Mountjoy, E. W. (1994). Rare earth element geochemistry of dolomites in the middle Devonian Presqu'ile barrier, Western Canada Sedimentary Basin: Implications for fluid-rock ratios during dolomitization. *Sedimentology*, *41*(4), 787–804.

Ramsey, J. M., & Chester, F. M. (2004). Hybrid fracture and the transition from extension fracture to shear fracture. *Nature*, *428*(6978), 63–66.

Root, K. G. (2001). Devonian Antler fold and thrust belt and foreland basin development in the southern Canadian Cordillera: Implications for the Western Canada Sedimentary Basin. *Bulletin of Canadian Petroleum Geology*, *49*(1), 7–36.

Rosenbaum, J., & Sheppard, S. M. F. (1986). An isotopic study of siderites, dolomites and ankerites at high temperatures. *Geochimica et Cosmochimica Acta*, *50*(6), 1147–1150.

Rustichelli, A., Iannace, A., Tondi, E., Di Celma, C., Cilona, A., Giorgioni, M., Parente, M., Girundo, M., & Invernizzi, C. (2017). Fault-controlled dolomite bodies as palaeotectonic indicators and geofluid reservoirs: New insights from Gargano promontory outcrops. *Sedimentology*, *64*(7), 1871–1900.

Ryan, B. H., Kaczmarek, S. E., Rivers, J. M., & Manche, C. J. (2022). Extensive recrystallization of Cenozoic dolomite during shallow burial: A case study from the Palaeocene–Eocene Umm er Radhuma formation and a global meta-analysis. *Sedimentology*, *69*, 2053–2079.

Ryb, U., & Eiler, J. M. (2018). Oxygen isotope composition of the Phanerozoic Ocean and a possible solution to the dolomite problem. *Proceedings of the National Academy of Sciences*, *115*(26), 6602–6607.

Ryb, U., Lloyd, M. K., Stolper, D. A., & Eiler, J. M. (2017). The clumped-isotope geochemistry of exhumed marbles from Naxos, Greece. *Earth and Planetary Science Letters*, *470*, 1–12.

Schulze, D. J., Harte, B., Valley, J. W., Brenan, J. M., & Dominic, M. D. R. (2003). Extreme crustal oxygen isotope signatures preserved in coesite in diamond. *Nature*, *423*(6935), 68–70.

Sharp, I., Gillespie, P., Morsalnezhad, D., Taberner, C., Karpuz, R., Vergés, J., Horbury, A., Pickard, N., Garland, J., Hunt, D. 2010. Stratigraphic architecture and fracture-controlled dolomitization of the cretaceous Khami and Bangestan groups: An outcrop case study, Zagros Mountains, Iran. In F. S. P. Van Buchem, K. D. Gerdes, & M. Esteban (Eds.), *Mesozoic and Cenozoic carbonate Systems of the Mediterranean and the Middle East: Stratigraphic and diagenetic reference models* (Vol. *329*, No. 1, pp. 343–396). Geological Society, Special Publications.

Shelton, K. L., Hendry, J. P., Gregg, J. M., Truesdale, J. P., & Somerville, I. D. (2019). Fluid circulation and fault- and fracture-related diagenesis in Mississippian Syn-rift carbonate rocks on the northeast margin of the Metalliferous Dublin Basin, Ireland. *Journal of Sedimentary Research*, *89*(6), 508–536.

Sibley, D. F., & Gregg, J. M. (1987). Classification of dolomite rock textures. *Journal of Sedimentary Research*, *57*, 967–975.

Slind, O. L., Andrews, G. D., Murray, D. L., Norford, B. S., Paterson, D. F., Salas, C. J., & Tawadros, E. E. (1994). Middle Cambrian to lower Ordovician strata of the Western Canada Sedimentary Basin. In G. Mossop & I. Shetsen (Eds.), *Geological atlas of the Western Canada Sedimentary Basin* (Special Report, Vol. *4*, pp. 87–108). Canadian Society of Petroleum Geologists and Alberta Research Council.

Stacey, J., Corlett, H., Holland, G., Koeshidayatullah, A., Cao, C., Swart, P., Crowley, S., & Hollis, C. (2021). Regional fault-controlled shallow dolomitization of the Middle Cambrian Cathedral formation by hydrothermal fluids fluxed through a basal clastic aquifer. *Geological Society of America Bulletin.*, *133*(11–12), 2355–2377.

Steele-MacInnis, M., Lecumberri-Sanchez, P., & Bodnar, R. J. (2012). Short note: HokieFlincs_H2O-NaCl: A Microsoft Excel spreadsheet for interpreting microthermometric data from fluid inclusions based on the PVTX properties of H2O-NaCl. *Computers & Geosciences*, *49*, 334–337.

Swennen, R., Dewit, J., Fierens, E., Muchez, P., Shah, M., Nader, F., & Hunt, D. (2012). Multiple dolomitization events along the Pozalagua fault (Pozalagua quarry, Basque–Cantabrian Basin, northern Spain). *Sedimentology*, *59*, 1345–1374.

Swennen, R., Vandeginste, V., & Ellam, R. (2003). Genesis of zebra dolomites (Cathedral formation: Canadian Cordillera Fold and Thrust Belt, British Columbia). *Journal of Geochemical Exploration*, *78*, 571–577.

Symons, D. T. A., Lewchuk, M. T., & Sangster, D. F. (1998). Laramide orogenic fluid flow into the Western Canada sedimentary basin; evidence from paleomagnetic dating of the kicking horse Mississippi valley-type ore deposit. *Economic Geology*, *93*(1), 68–83.

Taylor, S. R., & McLennan, S. M. (1985). *The continental crust: Its composition and evolution* (p. 312). Blackwell.

Tostevin, R. (2021). Cerium anomalies and paleoredox. In T. Lyons, A. Turchyn, & C. Reinhard (Eds.), *Elements in geochemical tracers in earth system science* (pp. 1–21). Cambridge University Press.

Tostevin, R., Shields, G. A., Tarbuck, G. M., He, T., Clarkson, M. O., & Wood, R. A. (2016). Effective use of cerium anomalies as a redox proxy in carbonate-dominated marine settings. *Chemical Geology*, *438*, 146–162.

Vandeginste, V., John, C. M., Cosgrove, J. W., & Manning, C. (2014). Dimensions, texture distribution, and geochemical heterogeneities of fracture–related dolomite geobodies hosted in Ediacaran limestones, northern Oman. *AAPG Bulletin*, *98*, 1789–1809.

Vandeginste, V., Swennen, R., Gleeson, S. A., Ellam, R. M., Osadetz, K., & Roure, F. (2005). Zebra dolomitization as a result of

focused fluid flow in the Rocky Mountains fold and Thrust Belt, Canada. *Sedimentology*, *52*, 1067–1095.

Vandeginste, V., Swennen, R., Gleeson, S. A., Ellam, R. M., Osadetz, K., & Roure, F. (2007). Geochemical constraints on the origin of the Kicking Horse and Monarch Mississippi Valley-type lead-zinc ore deposits, Southeast British Columbia, Canada. *Mineralium Deposita*, *42*(8), 913–935.

Veizer, J., & Prokoph, A. (2015). Temperatures and oxygen isotopic composition of Phanerozoic oceans. *Earth-Science Reviews*, *146*, 92–104.

Wallace, M. W., & Hood, A. v S. (2018). Zebra textures in carbonate rocks: Fractures produced by the force of crystallization during mineral replacement. *Sedimentary Geology*, *368*, 58–67.

Wallace, M. W., Both, R., Morales-Ruano, S., Hach-Ali, P. F., & Lees, T. (1994). Zebra textures from carbonate-hosted sulfide deposits: Sheet cavity networks produced by fracture and solution enlargement. *Economic Geology*, *89*, 1183–1191.

Wallace, M. W., Hood, A.v S., Shuster, A., Greig, A., Planavsky, N. J., & Reed, C. P. (2017). Oxygenation history of the Neoproterozoic to early Phanerozoic and the rise of land plants. *Earth and Planetary Science Letters*, *466*, 12–19.

Wheeler, J. O., Hoffman, P. F., Card, K. D., Davidson, A., Sanford, B. V., Okulitch, A. V., & Roest, W. R. (1996). Geological map of Canada. *Geological Survey of Canada, "A" Series Map*, *1860A*.

Woodhead, J. D., Hellstrom, J., Hergt, J. M., Greig, A., & Maas, R. (2007). Isotopic and elemental imaging of geological materials by laser ablation inductively coupled plasma-mass spectrometry. *Geostandards and Geoanalytical Research*, *31*(4), 331–343.

Yao, S., Gomez-Rivas, E., Martín-Martín, J. D., Gómez-Gras, D., Travé, A., Griera, A., & Howell, J. A. (2020). Fault-controlled dolostone geometries in a transgressive–regressive sequence stratigraphic framework. *Sedimentology*, *67*(6), 3290–3316.

SUPPORTING INFORMATION

Additional supporting information can be found online in the Supporting Information section at the end of this article.

How to cite this article: McCormick, C. A., Corlett, H., Clog, M., Boyce, A. J., Tartèse, R., Steele-MacInnis, M., & Hollis, C. (2023). Basin scale evolution of zebra textures in fault-controlled, hydrothermal dolomite bodies: Insights from the Western Canadian Sedimentary Basin. *Basin Research*, *00*, 1–30. https://doi.org/10.1111/bre.12789